Structure and dynamics of a muti-domain nitric oxide synthase regulated by a C2 domain

Dhruva Nair and Brian R. Crane*

AUTHOR ADDRESS:
Weill Institute for Cell and Molecular Biology
Department of Chemistry and Chemical Biology
Cornell University, Ithaca, NY 14853, USA.

*For correspondence: bc69@cornell.edu

Short Title: syNOS is a C2-domain-regulated multi-domain NOS.

Abstract

Nitric oxide synthase (NOS) is a widely studied multi-domain redox enzyme that produces the key signaling molecule and cytotoxic agent nitric oxide (NO) for functions that range from mammalian vasodilation to prokaryotic antibiotic resistance. NOS enzymes from metazoans and cyanobacteria rely on dynamic associations of their oxygenase and coupled di-flavin reductase domains that have largely evaded detailed structural characterization. CryoEM studies of a representative dimeric six-domain Synechococcus NOS reveal the architecture of the full-length enzyme, which contains an unusual regulatory C2 domain, and additional nitric oxide deoxygenase (NOD) and pseudo-globin modules. Five distinct structural states depict how pterin binding couples to tight and loose oxygenase conformations and how the Ca^{2+}-sensitive C2 domain moves over 85 Å to alternatively regulate either the NOS or NOD heme center. The extended C-terminal tail and its stabilizing interactions highlight an added layer of regulation required by multi-domain NOSs compared to other di-flavin reductases.

Teaser: syNOS is a highly dynamic multi-domain oxidoreductase that harnesses a Ca^{2+}-sensitive C2 domain to modulate activity.

Introduction

Nitric oxide (NO) is a potent free-radical signal and cytotoxic agent found throughout biology (*1–8*). Nitric Oxide Synthases (NOS) are homodimeric P450-like enzymes that produce NO through the 5-electron oxidation of L-arginine (L-arg) to L-citrulline (*9–12*). NOSs comprise a heme-containing oxygenase domain (NOS_{Oxy}) that is reductively activated by either an appended reductase domain (NOS_{Red}, characteristic of metazoans) or an auxiliary reductase partner (characteristic of prokaryotes) (Fig 1A) (*10–12*).

Mammalian NOSs (mNOSs) are multi-domain enzymes composed of an N-terminal NOS_{Oxy} and a C-terminal NADPH-dependent NOS_{Red}, bridged by a calmodulin (CAM)-binding domain (NOS_{CBD}; Fig. 1A). NOS_{Red} belongs to the cytochrome P450 reductase (CYPOR) family and as such, is further divided into a NOS_{Oxy}-proximal FMN-binding flavodoxin domain (NOS_{Fld}) and an FAD- and NADPH-binding ferredoxin-$NADP^+$ reductase module (NOS_{FNR}) (*10–13*). NOS_{Oxy} utilizes tetrahydrobiopterin (BH_4) or tetrahydrofolate for rapid heme reduction during oxygen activation (*14*). To reduce heme for oxygen binding, electrons flow from NADPH -> FAD -> FMN(H)• -> Heme-Fe^{3+}. Ca^{2+}- CAM enhances heme reduction by facilitating the traverse of NOS_{Fld} ~70 Å from a shielded position in a conformationally locked state of NOS_{Red} to a productive binding interaction with NOS_{Oxy} (*15–18*).

Given their medicinal importance (*19*), NOSs have been extensively studied in mammals, which have three isoforms: 1) endothelial NOS (eNOS, regulation of the vasculature), 2) neuronal NOS (nNOS, regulation of neuronal function), and 3) inducible NOS (iNOS, immune responses to pathogens and cancer cells) (*11*, *20–22*). Most prokaryotic NOSs have fewer domains than their metazoan counterparts and have diverse functions that include participation in stress responses, antibiotic resistance and biosynthesis of secondary metabolites (*23–27*).

To mitigate NO cytotoxicity, prokaryotes oxidize NO to NO_3^- with flavohemoprotein (Hmp), which combines a heme-reducing flavin reductase with an oxygen-activating globin domain. In contrast, mammals oxidize NO with hemoglobin, cytoglobin and neuroglobin, which obtain reduced equivalents from various environmental factors (*28–30*).

67 Cyanobacterial NOSs represent a bridge between metazoan and prokaryotic NOSs (*26*, *31–34*).
68 They comprise an mNOS architecture fused to an N-terminal globin domain, as exemplified by
69 the 1468-residue NOS from *Synechococcus sp*. PCC 7335 (i.e. syNOS, Fig. 1A). Like mNOS, Ca^{2+}
70 activates syNOS, despite syNOS lacking a CBD and Synechococcus lacking an obvious CAM
71 homolog (*34*). The syNOS globin domain (NOS_{Glb}) oxidizes NO to NO_3^- as a nitric oxide
72 dioxygenase (NOD) and, when considered with $syNOS_{FNR}$, resembles Hmp (*34*).

73 Ca^{2+}-CAM regulates mNOS activity by controlling the motions and associations of NOS_{Oxy} and
74 NOS_{Red} that allow electron transfer (ET) between them. Owing to the dynamic nature of
75 turnover and inactivated states of full-length NOSs, they have evaded characterization by direct
76 structural methods. Single particle electron microscopy (EM) in conjunction with chemical
77 crosslinking and hydrogen-deuterium exchange mass spectrometry (HDX-MS) have yielded
78 informative, if incomplete, structural information (*35–39*). These studies, along with
79 biochemical and spectroscopic characterization (*12*, *40–44*) have motivated a model of mNOS
80 conformational dynamics that involves three states: i) input, wherein NOS_{Fld} closely associates
81 with NOS_{FNR} so that the NOS_{Red} FAD can be reduced by NADPH; ii) intermediate, wherein NOS_{Fld}
82 transitions between its closed position next to NOS_{FNR} and an interaction with NOS_{Oxy}; and iii)
83 output, wherein Ca^{2+}-CAM promotes docking of NOS_{Fld} onto the NOS_{Oxy} of the adjacent subunit
84 (*44–47*). Although cryoEM has provided residue-level information on NOS_{Oxy}, NOS_{Red} positioning
85 has been challenging to discern owing to its conformational heterogeneity (*35*, *46*).

86 Herein, we resolve domain configurations of the multi-domain syNOS by cryoEM in conjunction
87 with further characterizing ET properties associated with its NOS and NOD activities. We
88 capture resting and dynamic states of the enzyme and identify an atypical C2-like domain that
89 acts as a reversible lynchpin to mediate Ca^{2+} sensitivity. An elaborated C-terminal tail (CTT) (*22*)
90 of NOS_{Red} , key for regulation of mNOS, maintains a conformationally locked dimer and
91 represents an expansion of the regulatory mechanisms seen within the di-flavin reductase
92 family.

93

94

Results and Discussion

SyNOS expression and purification

Full-length *Synechococcus PCC 7335* NOS was fused to an N-terminal-twin strep affinity tag and co-expressed along with *E. coli* HSP90 and GAPDH, in BL21(DE3) and purified through a series of affinity and size exclusion columns (SEC) (see Methods, Fig. S1) (*46*, *48*, *49*). As found previously (*34*), syNOS purified as a mixture of monomers and dimers. SEC fractions were tested for NO production with L-arg and NADPH and active fractions were applied to glow-discharged Cu-Quantifoil grids, vitrified and imaged on either a Talos Arctica or Titan Krios. Prior to freezing, samples were incubated with or without Ca^{2+}/L-arg/NADPH (Table S1).

Structure determination of inactivated full-length syNOS

SyNOS data sets and the states within are summarized in Table S1 and described below. Two datasets of syNOS samples lacking Ca^{2+}, L-arg and NADPH were collected on a Talos Arctica equipped with a K3 detector. Dataset (DS) 1 (1215 micrographs) and DS2 (4055 micrographs) were initially preprocessed using CryoSPARC (Fig. S2 and S3), then subjected to particle picking using CRYOLO and finally refined in CryoSPARC (*50*, *51*). During 2D classification multiple classes emerged resembling a symmetric full-length dimer (NOS-Sym). DS1 produced a NOS-Sym overall resolution of 3.8 Å (47 K particles), and DS2 produced a NOS-Sym map of 4.7 Å resolution (84 K particles).

In addition, an asymmetric class (NOS-Asym) became apparent in both DS1 and DS2 that lacked density for one $syNOS_{Red}$ and one $syNOS_{C2}$. DS1 produced a NOS-Asym map with the nominal resolution of 3.67 Å (67 K particles), whereas DS2 yielded a 4.00 Å resolution map (265 K particles). In NOS-Asym, uninterpretable electron density surrounds the position of the vacated $syNOS_{Red}$ indicative of conformational disorder for this subunit.

3D-refinement of NOS-Sym gave clear electron density for secondary structure, cofactors and in many cases, residue side chains. Portions of each subunit were less well defined yet still allowed unambiguous placement of the constituent domains. Inspection of the electron density indicated that the homodimer interface was structurally heterogeneous. To better reconstruct

122 the full-length dimer, we combined the NOS-Sym particle stacks from DS1 (47 K particles) and
123 DS2 (84 K particles) and re-refined the density alignment for 3D-variability (VA) and 3D-Flex
124 analysis. We explored C1, C2 and C2 (relaxed) symmetries which yielded 3.99 Å, 3.95 Å and 3.95
125 Å nominal resolutions, respectively, with the C2(relaxed) refinement chosen for further
126 flexibility analysis (Fig. S4, discussed below). The C2 symmetry-imposed electron density was
127 sufficient for model building and refinement (Table S2).

128

129 <u>Structure determination of turnover syNOS</u>

130 DS3 (Fig. S5) (5019 micrographs) represented syNOS incubated with Ca^{2+}, BH_4, L-arg and NADPH
131 and was collected on a Titan Krios equipped with a K3 detector. Micrographs were initially
132 preprocessed using CryoSPARC (Fig. S5), then subjected to particle picking with CRYOLO and
133 finally refined in CryoSPARC. During 2D classification, multiple classes emerged resembling NOS-
134 Asym but also a state that lacked density for $syNOS_{Red}$ on both subunits. The latter state
135 resembles previously determined nNOS cryoEM structures that resolved a NOS_{Oxy} homodimer
136 but lacked density for $nNOS_{Red}$ owing to conformational disorder (*36*). We refer to this class as
137 the a "loose" turnover state ($NOS\text{-}TO_L$), because the NOS_{Oxy} interface is expanded relative to a
138 typical "tight" $mNOS_{Oxy}$ dimer. 2D classes of $NOS\text{-}TO_L$ gave density plumes at the interface
139 characteristic of poor signal alignment, indicative of a conformationally heterogeneous particle,
140 hence a composite map from two local refinements was created. NOS-Asym was refined to a
141 nominal resolution of 3.19 Å (71 K particles), whereas $NOS\text{-}TO_L$ was resolved to 3.6 Å resolution
142 (61 K particles, Table S2).

143

144 DS4 was collected from the same conditions on the 200 KV Talos Arctica equipped with a K3
145 detector. These grids, which had thicker crystalline ice, produced an intermediate resolution
146 turnover state with a tight NOS_{Oxy} dimer interface ($NOS\text{-}TO_T$) that more closely resembles crystal
147 structures of BH_4-bound $mNOS_{Oxy}$ (Fig. S6).

148

149 Structure determination of monomeric syNOS in turnover conditions

150 DS5 (9036 micrographs) of syNOS incubated with BH_4, Ca^{2+}, L-arg and NADPH was collected on a
151 Titan Krios equipped with a Falcon 3 detector (Fig. S7). For this dataset, the homodimers
152 appeared primarily dissociated into monomers (NOS-Mon). Unlike NOS-Asym, in NOS-Mon,
153 even NOS_{Oxy} appeared as a monomer. The micrographs were processed through CryoSPARC with
154 multiple rounds of 3D particle stack cleaning to remove damaged particles (Fig. S7). The syNOS
155 monomer density was refined to 3.09 Å resolution (45 K particles), with discernible sidechains
156 and cofactors, although neither Ca^{2+}, nor L-arg could be identified in the map (Table S2).

157

158 Full-length syNOS ($syNOS_{FL}$) molecular architecture

159 In the absence of Ca^{2+}, the NOS-Sym state of the full-length enzyme ($syNOS_{FL}$) forms a compact
160 C2-symmetric homodimer composed of six domains per subunit (Fig. 1B,C,D); the domain
161 arrangements divide the protein into two redox modules: i) an Fld-FNR module with an N-
162 terminal C2 domain (residues 1-134) bound at the Oxy-FNR interface and ii) a Glb-Oxy module,
163 that also contains an 8-helical pseudo-globin domain that does not bind heme ($syNOS_{pGlb}$,
164 residues 179-339). Three extended linkers connect the most mobile domains, with L1 (44
165 residues) connecting NOS_{C2} to NOS_{pGlb}, L2 (10 residues) connecting NOS_{Oxy} to NOS_{Fld} and L3 (13
166 residues) connecting NOS_{Fld} to NOS_{FNR} (Fig. S8).

167 In this symmetric "locked" state, syNOS dimerizes through interactions of $syNOS_{Oxy}$ (residues
168 474-852), and $syNOS_{pGlb}$, which bridges the gap between $syNOS_{Glb}$ (residues 340-473) and
169 $syNOS_{Oxy}$ (Fig. 1B, C). $SyNOS_{pGlb}$ lacks discernible density for an insertion between αD/ αE
170 (residues 245-263), which would superimpose on the position of the zinc-binding site found in
171 the $mNOS_{Oxy}$ dimer; the zinc site is not contained in syNOS (Fig. S9 A, B, C). The $syNOS_{Oxy}$ C-
172 terminal helical hairpin acts as an interaction hub at the center of the subunit by contacting
173 NOS_{Fld}, NOS_{FNR}, NOS_{Glb} and the C2 domain.

174 All structures, except for NOS-TO_T, lacked density for the helical lariats or BH_4, which compose
175 the center of the NOS_{Oxy} dimer interface (Fig. S9). However, 3D variable analysis (3DVA) and 3D

176 Flexible refinement (3DFlex) conducted on NOS-Sym, revealed that syNOS subunits "breathe"
177 between tight, ordered associations that bind BH_4 within the helical lariats and more separated
178 looser associations with weak density for these regions (Movie S1), not unlike the "tight" and
179 "loose" dimer states previously observed for *B. subtilis* NOS (*52–54*). Samples collected in
180 thicker ice favored the tight association (NOS-TO_T) for reasons unclear. In addition to an ordered
181 NOS_{Oxy} interface and density for BH_4, NOS-TO_T displayed new contacts between L1 and αA
182 ($syNOS_{pGlb}$) on one subunit and α9 ($syNOS_{Oxy}$) on the opposing subunit. Hence, L1 may influence
183 NOS_{pGlb} positioning, which in turn propagates structural stability to the dimer interface (Fig.
184 S9B).

185 The previously unannotated and uncharacterized N-terminal domain (residues 1-134) takes the
186 form of a tightly packed 8-stranded β-sandwich, capped by peripheral loops at each end (Fig.
187 1C, D). This structure strongly resembles a C2 domain ($syNOS_{C2}$), which is usually associated
188 with Ca^{2+}-dependent membrane targeting in eukaryotes and typically not found in prokaryotes.
189 (*55*, *56*) $SyNOS_{C2}$ brackets the backside of the $syNOS_{Oxy}$ heme pocket and $syNOS_{FNR}$ (residues
190 1017-1468; Fig. 1C). In NOS-Sym, $syNOS_{FNR}$ latches onto $syNOS_{Glb}$ through the ordered CTT,
191 which also binds to $syNOS_{Fld}$ (residues 863-1003; Fig. 1B, C).

192 $SyNOS_{Fld}$ and $syNOS_{FNR}$ comprise a canonical NOS reductase unit in a closed conformation with
193 the FMN-FAD isoalloxazine cofactors aligned in a planar end-to-end configuration (Fig. 2). To
194 facilitate ET between subunits, mNOSs rearrange to position NOS_{Fld} domain < 15 Å from the
195 $syNOS_{Oxy}$ heme on the opposing subunit (*57*). Residue conservation, cross-linking and HDX-MS
196 indicate that NOS_{Fld} interacts dynamically on the backside of the heme pocket at a conserved
197 Trp residue (356 in human eNOS) (*36–38*, *54*). $SyNOS_{C2}$ blocks this position and would have to
198 move to allow productive ET from $syNOS_{Fld}$, which also must displace from its shielded
199 interaction with $syNOS_{FNR}$ (*38*). Notably, syNOS lacks the mNOS CBD (~30 residues) that upon
200 CAM binding favors the ET competent 'output state' (Fig. 2A-C) (*17*, *38*, *58*, *59*). However, the
201 syNOS interdomain linkers also likely mediate domain motions. These linkers generally have
202 extended conformations, with the longest, L1, traversing ~60 Å. The threading of L1 beneath L2
203 implies that any C2 movement will displace L2 and thereby cause $syNOS_{Fld}$ to move "up-and-
204 over" toward the adjacent $syNOS_{Oxy}$ subunit (Fig. S8). In comparison to the interdomain

205 interactions implied by the 25 Å resolution nNOS + CAM structure by negative-stain EM (*37*),
206 $syNOS_{Fld}$ likely undergoes a different trajectory to interact with $syNOS_{Oxy}$ in part because
207 $syNOS_{Glb}$ will block the CAM-directed conformational change proposed for nNOS.

208

209 <u>$SyNOS_{Red}$ is distantly related, but structurally similar, to cytochrome P-450 reductase (CYPOR)</u>

210 $SyNOS_{Red}$, $mNOS_{Red}$, sulfite reductase diflavin reductase (SIRFP), and methionine synthase
211 reductase (MTRR) belong to the cytochrome P450 reductase (CYPOR) family of di-flavin
212 reductases (Fig. S10) (*60–63*). Di-flavin reductases perform three-separate ET reactions i)
213 hydride transfer from NADPH/NADH to the FNR FAD cofactor ii) sequential ET from the FNR to
214 the Fld iii) ET from the Fld to an enzymatically relevant electron sink. Activities (i) and (ii) occur
215 when the di-flavin reductase is trapped in a "closed" conformation permitting first hydride and
216 then electron transfer along the sequence NADPH->FAD->FMN(H)• with activity (iii) requiring an
217 "open" conformation that frees the Fld to reduce the electron sink (e.g. NOS_{Oxy} or cytochrome
218 c).

219 We sought to place $syNOS_{Red}$ within the genetic and structural context of other di-flavin
220 reductases by subjecting the $syNOS_{Red}$ protein sequence to clustering, phylogenetic estimation
221 using maximum likelihood (PhyML) and multiple protein structure alignments (MSTA). Sequence
222 analyses indicated that $syNOS_{Red}$ and $mNOS_{Red}$ are outgroups relative to CYPORs (Fig. S11); yet,
223 $syNOS_{Red}$ is more closely related in structure to CYPOR than to $nNOS_{Red}$ or other di-flavin
224 reductases (Fig. 2 and S10) (*22*). Nevertheless, key differences arise in the structural and
225 electrostatic features that stabilize the reductase closed conformation in syNOS (NOS-Sym)
226 compared to CYPOR (Fig. 2A-C).

227 The di-flavin closed conformation is defined by the L3 loop (situated between the Fld and the
228 FNR domain, blue in Fig. 2A, B), the Fld domain, and what we define as Interfacing Region (IR) 1,
229 IR2 and the CTT-IR. IR1 of CYPOR is comprised of an acidic patch surrounding the $CYPOR_{Fld}$ FMN
230 cofactor and a basic patch surrounding the $CYPOR_{FNR}$ FAD cofactor (Fig. 2C). $mNOS_{Red}$ retains a
231 homologous acidic/basic IR1 (Fig. 2B). CYPOR and mNOS conserve a hydrogen binding network
232 between the FNR control region and the Fld (Fig. 2A-C). $SyNOS_{Red}$ lacks electrostatic

complementarity to mediate IR1 and residue complementary to maintain IR2. (In syNOS, IR2 is composed of Fld residues Gly922/Leu920 binding against Trp1140/Glu1136 on the control region; whereas in CYPOR, IR2 is composed of Fld Glu213 hydrogen bonding with Arg382/Thr383). Hence, rather than IR1 and IR2, the CTT-IR and the C2 domain primarily stabilize the $syNOS_{Red}$ closed conformation (Fig. 3A).

$syNOS_{Red}$ and $mNOS_{Red}$ share a β-finger (syNOS residues 1100-1132) and a CTT that are important for redox flux in NOS but are not found in canonical CYPORs (Fig. 2A-C) (*22*, *46*). $syNOS_{Red}$ control region residues 1113-1132, which follow the β-finger, interact with the basic Fld loop (residues 888-891) to substitute for a CYPOR-like IR2. In syNOS, the β-finger is closer to the Fld domain (~7.5 Å) compared to in $mNOS_{Red}$ (~17 Å), thereby suggesting either a different structural role for this element or revealing a conformational state that $nNOS_{Red}$ can also assume (Fig. 2C). $syNOS_{Red}$ also lacks the $mNOS_{Red}$ Fld autoinhibitory regulatory loop (AI, nNOS residues 836-849) that destabilizes CAM binding at low levels of Ca^{2+} (Fig 2B) (*60*, *64*). Although syNOS, $nNOS_{Red}$, and CYPOR stabilize their closed conformations through different interactions, they all produce a coplanar orientation and similar separation between the FAD and FMN cofactors (~13 Å from flavin N5-to-N5).

<u>NOS CTTs are enzyme-specific conformational regulators</u>

CTTs, thought to be an mNOS addition within the conserved CYPOR family (*65*), are 20-30 residue helical extensions that auto-inhibit reduction of NOS_{Fld} by NOS_{FNR} (Fig. 3). Sequence alignments show no discernable residue similarity between the syNOS CTT and CTTs of the three mNOS isoforms or that of the most similar eukaryotic NOS sequence from the diatom *T. minus* NOS (Fig. S11). The lack of sequence similarity between $syNOS_{CTT}$ and $mNOS_{CTT}$, despite substantial similarity in the preceding $syNOS_{FNR}$ domains, implies convergent evolution of these CTTs, likely in concert with the addition of $syNOS_{Glb}$.

Unlike previous NOS_{Red} structures that capture only a portion of the CTT, the syNOS structure resolves the entire CTT and its interactions with $syNOS_{FLd}$ and $syNOS_{Glb}$ (Fig. 3). Compared to other NOSs, the 27-residue syNOS CTT can be divided into two perpendicular helices (CTT_1 and

261 CTT_2; residues 1440-1468; Fig. 3A). Several interactions provided by CTT_1 lock the position of
262 $syNOS_{Fld}$ in the canonical FNR-Fld closed conformation. CTT_1 (residues 1446-1458) interacts with
263 the FMN ligating loops of NOS_{Fld} (residues 984-989 and 951-960). In this interface, key residue
264 contacts likely influence ET-competent conformational states of $syNOS_{Fld}$ (e.g. Glu1454 salt-
265 bridges to Lys987, Tyr1458 hydrogen bonds with Asp984; and Asn1457 hydrogen bonds with
266 Thr953 (Fig. 3C-D)). Of these residues, CTT_1 Lys987 likely modulates Fld dynamics because it is
267 flanked by residues that coordinate the FMN pyrophosphate groups (Gln989 and
268 Glu985). Indeed, the Lys987Ala variant, which disrupts the Lys987/Glu1454 salt-bridge, has a
269 much more extended, flexible structure by small angle X-Ray scattering (SAXS) than does the WT
270 (Fig. S12).

271 The second CTT helix (CTT_2, residues 1460-1468) is absent in other NOSs and CYPORs, likely
272 because it binds to the atypical NOS_{Glb} (Fig. 3A). Indeed, an aliphatic patch on CTT_2 interacts
273 with the hydrophobic crevice between residues 358-392 on $syNOS_{Glb}$ (Fig 3A-B). Key interactions
274 between CTT_2 and NOS_{Glb} include Arg1460 hydrogen bonding to the mainchain carbonyl of
275 Arg382 and the mainchain carbonyl of Asn1457 hydrogen bonding with the side chain of
276 Arg382. FNR Lys1412 caps the carboxy-terminus of CTT_2 with a supporting interaction provided
277 by a hydrogen bond between Trp1464 and the FNR His1412 (Fig. 3E). Thus, CTT_1 and CTT_2
278 stabilize the associations of NOS_{Fld}, NOS_{FNR}, and NOS_{Glb} domains in the Ca^{2+}-free closed
279 conformation of syNOS.

280 $SyNOS_{Red}$ has distinct reactivity toward the surrogate electron acceptor cytochrome c (Cc),
281 compared to other CYPOR family members, including $mNOS_{Red}$. In the absence of Ca^{2+}, removal
282 of the CTT does not affect Cc reduction by syNOS (Fig. S13). Ca^{2+} decreases Cc reduction by
283 almost 4-fold, but, in contrast to the Ca^{2+}-depleted condition, removal of the CTT reactivates Cc
284 reduction (Fig. S13). In mNOS, CTT removal also activates Cc reduction, but Ca^{2+}-CAM further
285 increases, rather than decreases activity (*66*, *67*). Furthermore, replacing the $mNOS_{FNR}$ domain
286 with $CYPOR_{FNR}$, which lacks a CTT, switches the Ca^{2+}-CAM dependence of mNOS such that Cc
287 reduction now decreases ~4-fold with Ca^{2+}-CAM (*66*, *67*), much like for syNOS+Ca^{2+}. Thus, the
288 CTT reduces NOS_{Fld} interaction with Cc in both syNOS and nNOS, but the Ca^{2+} dependence is
289 opposite. These Cc reduction behaviors among NOS proteins likely reflect differences in the

290 relative strength of interactions among NOS_{Fld}, NOS_{FNR}, the CTT, NOS_{Oxy} and Cc
291 itself. Interestingly, syNOS structures in the Ca^{2+}-depleted states (NOS-Sym, NOS-Asym, NOS-
292 Mon) revealed a stable, closed Fld, whereas the Ca^{2+} turnover states (NOS-$TO_{1,2}$) had a mobile
293 undiscerned Fld domain, seemingly *more* conducive to Cc reduction, not less. However, in NOS-
294 TO, the Fld domain may partition more frequently toward NOS_{Oxy}, which would compete with Cc
295 and thereby reduce Cc reduction rates. In mNOS, relieving a stronger CTT-to-Fld interaction with
296 Ca^{2+}-CAM may favor the Fld-to-Cc interaction if the Fld-to-Oxy interaction is weaker than in
297 syNOS.

298 <u>$SyNOS_{Red}$ has distinct flavin reduction behavior</u>

299 $SyNOS_{FL}$ and $syNOS_{Red}$ rates of flavin reduction by NADPH, measured through anaerobic
300 stopped-flow experiments, were biphasic and resembled the flavin reduction kinetics of CYPOR
301 and $nNOS_{Red}$ bound to Ca^{2+}-CAM (Fig. S14A). The fast phase of $syNOS_{Red}$ reduction that accounts
302 for 90% of the amplitude change and corresponds to FAD reduction by NADPH has a pseudo
303 first order rate constant of k_1 ~178 s^{-1}, which is 4-fold greater than that of CYPOR (~42 s^{-1}) (*68*).
304 The slow phases for syNOS and CYPOR are nearly identical with k_2 ~4 s^{-1}. In contrast, the fast
305 phase of flavin reduction in $nNOS_{Red}$ (+ Ca^{2+}-CAM) is 3.5-fold greater than that of $syNOS_{Red}$.
306 Notably NADPH reduces $syNOS_{FL}$ at a ~74-fold slower rate than $syNOS_{Red}$ implying that the
307 closed conformation of $syNOS_{FL}$ restricts hydride transfer from NADPH to FAD (Fig. S14B-D).

308 The lower FAD reduction rate in $syNOS_{FL}$ is surprising because $syNOS_{Red}$ lacks an NADP(H)-
309 ligating Arg (1400 in rat nNOS) known to inhibit electron flow in CAM-free nNOS/eNOS (*69*). In
310 nNOS, the Arg1400Ser substitution increases flavin reduction while decreasing NO synthesis
311 (*69*). Because syNOS does not conserve the Arg1400 interaction (the corresponding residues is
312 an Asn) it would be predicted to have a slower flavin reduction rate than NOS_{Red} (*69*). However,
313 the NOS_{Glb}-to-CTT interaction, unique to syNOS, may especially stabilize conserved CTT residue
314 Trp1440 (*70*). As observed in the higher resolution structure of NOS-Mon, Trp1440 blocks the
315 nicotinamide group of NADPH from approaching the FAD isoalloxazine ring for hydride transfer
316 (Fig. S14B). The CTT enforced rigidity in syNOS may compensate for the modified $NADP^+$-binding
317 pocket that lacks an autoinhibitory Arg1400 equivalent. Notably, compared to nNOS and CYPOR

318 the nicotinamide moiety in syNOS adopts an atypical conformation that is intermediate to the
319 reduction incapable $NADP^+$ conformation seen in nNOS (PDB:1TLL) and the $NADP^+$/FAD stacked
320 conformation seen in the CYPOR W677X truncations (PDB:1AJO, Fig. S14D).

321

322 <u>Ca^{2+} regulates syNOS activity through a C2-like domain</u>

323 The lack of a CAM-CBD interaction in syNOS renders its Ca^{2+}sensitivity enigmatic. However,
324 $syNOS_{C2}$ structurally resembles C2 domains that mediate membrane recruitment by binding
325 Ca^{2+} (Fig. 4) particularly; mouse perforin C2 (Fig. 4A) (*55*, *56*, *71*).

326 In the closed conformation, $syNOS_{C2}$ forms a tripartite interface with the $syNOS_{Oxy}$ domain and
327 the FNR control region (Fig. 4B). Two regions of salt-bridges mediate the C2-Oxy interface. The
328 first (Fig. 4B), involving NOS_{C2} Arg107 and NOS_{Oxy} Glu568, reside beside Trp715, whose analog in
329 mNOS facilitates interactions important for ET from NOS_{Fld} (*38*). Asn575 further facilitates the
330 contact by stabilizing the Arg107 guanidium group for interaction with Glu568. The second
331 interface (Fig. 4B) involves the NOS_{Oxy} αA-to-αB loop and C2 the β4-β5 connection. C2 Arg57
332 salt-bridges with Glu523 in an interaction that is buttressed by an amide sidechain of Gln494. A
333 basic patch on the C2-domain and a complementary acidic patch on α-helix 1162-1173 of the
334 FNR-control domain wedges the C2 between NOS_{Oxy} and NOS_{Fld} (Fig. 4C). Because $syNOS_{C2}$
335 blocks the putative Fld-Oxy contact; displacement of $syNOS_{C2}$ would decrease conformational
336 restraints on $syNOS_{Red}$ (particularly the L2 linker) and relieve steric hindrance on the backside of
337 the heme pocket.

338 Removal of the C2 domain ($syNOS_{\Delta C2}$, residues 179-1468) abrogates NOS activity but retains Cc-
339 reduction activity (Fig. S13). Strikingly, $syNOS_{\Delta C2}$ has a high WT-like Cc-reduction rate that is
340 uninhibited by Ca^{2+}. In keeping with an enzyme unconstrained by inhibitory interactions, SAXS
341 data indicates that the global flexibility of $syNOS_{\Delta C2}$ exceeds that of the WT and the more
342 flexible K987A variant (Fig. S13). Thus, the C2 domain influences redox domain mobility of
343 syNOS in response to Ca^{2+}, akin to the functional role that Ca^{2+}-CAM plays in the regulation of
344 mNOSs. In other systems, Ca^{2+} binding to C2 domains neutralizes acidic regions to allow

345 association with negatively charged phospholipid head-groups (*72*). Although, $syNOS_{C2}$ lacks
346 the typically conserved Asp residues that coordinate Ca^{2+}, isothermal calorimetry (Fig. S15)
347 indicated that the $syNOS_{C2}$ binds Ca^{2+} with a 1.6 μM Kd, which compares to the Ca^{2+} affinity of
348 PLDβ C2 domains (0.8 μM) (*73*).

349

350 <u>Ca^{2+} causes a large movement of the C2 domain</u>

351 In the presence of Ca^{2+} and L-arginine, syNOS adopts a more flexible state, wherein most of
352 NOS_{Red} is undiscerned by cryoEM (NOS-$TO_{L,T}$). In this turnover state, the C2 domain has moved
353 away from the Oxy/FNR interface and now binds at the entrance of the $syNOS_{Glb}$ heme pocket,
354 nearly 85 Å from its original position (Fig. 5A). The new C2 position blocks the $syNOS_{Glb}$ heme-
355 binding center and substantially shifts the αB-D helices and constituent residues that compose
356 the distal heme pocket where NO is oxidized (Fig. 5B). The highly conserved C2 basic patch
357 (Lys35, Lys37 and Arg81) that formally bound NOS_{FNR} in the locked dimer interacts with the
358 heme-propionic acid groups of NOS_{Glb} and the 81-89 loop, also conserved among NOS_{C2}
359 domains, reaches over to block the distal heme pocket. Furthermore, the movement of NOS_{C2}
360 displaces the L2 linker, which swivels by ~135° and now directs $syNOS_{Fld}$ toward the backside of
361 the heme pocket on the opposing subunit (Fig. 5C), consistent with the trans ET mechanism
362 characteristic of mNOSs (*57*). As $syNOS_{C2}$ now resides where the electron-donating FNR
363 modules of Hmps interact with their cognate globin domains we tested whether removal of the
364 C2 domain ($syNOS_{\Delta C2}$) affected $syNOS_{Glb}$ reduction in $syNOS_{FL}$. Surprisingly, we observed little
365 change in $syNOS_{Glb}$ reduction rates in $syNOS_{\Delta C2,}$ nor did Ca^{2+} affect $syNOS_{Glb}$ reduction rates in
366 $syNOS_{FL}$ (Fig. S14).

367 $syNOS_{FNR}$ and $syNOS_{Fld}$ have 2-electron reduction potentials characteristic of flavodoxin
368 domains. Considering that $syNOS_{Glb}$ has a lower potential ($E^{0'}$ = -250 mV) than $syNOS_{Fld}$ ($E^{0'}$ = -
369 170 mV), but not $syNOS_{FNR}$ ($E^{0'}$ = -290 mV), if a hydroquinone state reduces the globin, $syNOS_{FNR}$
370 is likely the better donor. Moreover, a difference of ~40 mV between $syNOS_{FNR}$ and $syNOS_{Glb}$
371 (Table S4), a typical reorganization energy of ~ 1.0 eV and a distance of separation of ~31 Å,
372 suggests that $syNOS_{FNR}$ displaces from its position in NOS-Sym to reduce $syNOS_{Glb}$ at the

373 observed rates (Fig. 6).(*74*) A modest decrease in syNOS NOD activity with Ca^{2+} suggests an
374 inhibitory effect of $syNOS_{C2}$ (Fig. S16). $SyNOS_{\Delta C2}$ again showed little change relative to $syNOS_{FL}$,
375 but note that this variant is also inactive for NO synthesis. A difference in $syNOS_{Glb}$ reactivity in
376 $syNOS_{\Delta C2}$ may not be pronounced because the cryoEM data reveals that the protein is never in a
377 pure conformational state; and the exchange rates among conformational states may exceed
378 the interdomain reduction rates. In vivo, other factors may stabilize the turnover vs the locked
379 states of syNOS and produce tighter regulation among them.

380

381 <u>The asymmetric state may act as a conformational intermediate between NOS and NOD</u>
382 <u>activities</u>

383 The mNOS input, intermediate, and output states are not discrete, but sampled within a
384 continuum of motion (*18*, *35*). In the output state, Fld-CAM moves 70 Å to dock onto an
385 opposing NOS_{Oxy} domain at the backside of the heme pocket. Similarly, the syNOS flexible
386 asymmetric dimer class (NOS-Asym) represents an intermediate structural state between the
387 locked dimer and the turnover state that is likely in equilibrium with NOS-Sym and NOS-TO. An
388 Alphafold3 prediction of the pGlb-Glb-Oxy dimer unit with one Fld domain places NOS_{Fld} at the
389 experimentally validated position on NOS_{Oxy} found by HDX-MS and crosslinking studies of mNOS
390 (*38*). Upon superimposing this prediction onto either NOS-Asym or NOS-Sym, the Fld binding
391 surface on NOS_{Oxy} is blocked by the NOS_{C2} (Fig. 5C and S17). Furthermore, compared to Hmp,
392 $syNOS_{FNR}$ would have to rotate 90° and move 28 Å to reduce $syNOS_{Glb}$ (Fig. 6). This configuration
393 is likely accessible in the dynamic asymmetric subunit but would not be possible in NOS-TO
394 because of the rearranged $syNOS_{C2}$. Hence, it is likely that NOS-Asym is capable of $syNOS_{Glb}$
395 reduction but not $syNOS_{Oxy}$ reduction.

396 The intermediate conformation of NOS-Asym may be important for the switch between NOS
397 and NOD activities and explain the inhibitory effect of Ca^{2+} on Cc-reduction. In the absence of
398 Ca^{2+}, NOS-Sym locks down and inhibits NOS activity, but NOS-Asym allows $syNOS_{FNR}$ to reduce
399 $syNOS_{Glb}$, and $syNOS_{Fld}$ to reduce Cc. In NOS-Asym, $syNOS_{Fld}$ cannot reduce $syNOS_{Oxy}$ because
400 $syNOS_{C2}$ blocks $syNOS_{Fld}$ from the $syNOS_{Oxy}$ interaction site on the opposing subunit. Ca^{2+}

401 promotes the relocation of the C2 domain from $syNOS_{Oxy}$ to $syNOS_{Glb}$; however, some C2
402 displacement from NOS_{Oxy} may occur in the absence of Ca^{2+} because the C2 domain is not well
403 defined in the more mobile subunit of NOS-Asym. In addition to preventing $syNOS_{FNR}$ from
404 reducing the $syNOS_{Glb}$, C2 movement disrupts L2, destabilizing the interaction of NOS_{Fld} with
405 NOS_{FNR} and favors partitioning of NOS_{Fld} toward the unblocked NOS_{Oxy} and away from Cc (Fig. 7).
406 Similar to mNOS, syNOS assumes a continuum of conformations that circumscribe defined
407 enzymatic states. Hence to generate changes in physiologically relevant activities, the relative
408 weighting of states within the conformational ensemble must be regulated and responsive to
409 cellular context. It is striking that the $syNOS_{C2}$ moves between a location that blocks $syNOS_{Oxy}$
410 reduction to one that blocks $syNOS_{Glb}$ reduction, thereby suggesting counter regulation of NO
411 synthesis and NO oxidation. Such a mechanism may allow the enzyme to tune the balance of
412 NO production versus NO detoxification, which would be of benefit for signal transduction,
413 nitrogen metabolism and cellular homeostasis. Overall, these syNOS structural studies
414 demonstrate how a multi-domain reductase and its associated regulatory components can
415 undergo large scale rearrangements to modulate reactivity in response to environmental
416 conditions.

417

418 **Methods**

419 **Molecular cloning**

420 The native coding sequence for full-length syNOS (Uniprot ID : B4WU43**)** was PCR-amplified and
421 cloned into a modified pet28-a construct between restriction sites NdeI and XhoI using
422 NEBuilder HiFi DNA Assembly master mix (E2621L). The construct contained sequences for an
423 N-terminal Twin-Strep Tag with a TEV cleavage site. To produce the hptG and gapA construct,
424 htpG and gapA were amplified from K-12 *E. coli* and placed into the MCS-1 and the MCS2 of a
425 tagless pAYC-Duet vector using NEBuilder HiFi DNA Assembly master mix (E2621L). Individual
426 point mutants were constructed using Kinase-Ligase-DpnI (KLD) method using primers in
427 supplementary Table 3 (New England Biosciences). All plasmid molecular cloning and plasmid
428 material generation were carried out with NEB® 5-alpha competent *E. coli* (New England

429 Biosciences). Successful transformants were validated through Sanger Sequencing or Nanopore
430 sequencing (Eurofins Genomics).

431 **Protein expression and purification**

432 SyNOS and/or variants were expressed in BL21(DE3) as previously described (*34*) with the
433 modification of co-expression with hptG/gapA, which improved yield and reproducibility. Cell
434 pellets were stored at -80 ^{o}C prior to purification. The pellet was thawed and resuspended in
435 lysis buffer (50 mM HEPES (pH 7.5), 150 mM NaCl, 1 mM TCEP, 10% glycerol and 10 uM BH_4),
436 followed by high-speed centrifugation at 100 000 G and application on Strep-Tactin XT 4-Flow
437 resin (IBA Life Sciences). Elution of the affinity-bound protein fraction was carried out in batch
438 with 50 mM biotin supplemented lysis buffer. Post elution samples were concentrated using
439 Viva-Spin columns (100 kDa cut -off), before application onto 10/300 Superose 6 Increase
440 Column (Cytiva) using Gel Filtration Buffer 1(GFB1, 25 mM HEPES (pH 7.5), 150 mM NaCl, 1 mM
441 TCEP, 10% glycerol and 10 uM BH_4).

442 **Size exclusion chromotography - Small angle X-ray scattering (SEC-SAXS)**

443 All SEC-SAXS was performed at ID7A1 beamline at Cornell High Energy Synchrotron Source
444 (CHESS). Photon flux was 2.3 x 10^{12} ph/s and scattering data was collected 0.005 $Å^{-1} \leq q \leq 0.7$ $Å^{-1}$
445 on an EIGER 4M detector (Dectris). Samples were injected into an inline 3.2/150 Superdex 200
446 column in gel filtration buffer. The entire SEC-SAXS trace was captured using a 2s exposure. All
447 SEC-SAXS data processing was performed through RAW (*75*).

448 **Single turnover anaerobic globin reduction**

449 Anerobic $syNOS_{Glb}$ heme reduction assays were carried out using an Agilent 8453 UV-Vis
450 spectrometer with an attached Hewlett Packard 89090A Peltier temperature controller for
451 maintaining constant temperature at 20 ^{o}C and constant stirring at 400 rpm (Agilent & Hewlett
452 Packard). Prior to reaction initiation with 1 mM NADPH, syNOS or variants (1 µM) were
453 incubated anaerobically in the presence of the Glucose Oxidase/Catalase (GOD/CAT) oxygen
454 scavenging system, as previously described (*76*). Samples were run in either in the presence of 1

455 mM Ca^{2+} or 1 mM EGTA, as noted. All data was processed using home-made scripts in R Studio
456 (Posit PBC).

457 **Stopped-flow pre-steady state flavin reduction kinetics**

458 Anerobic stopped-flow mixing of NADPH with $syNOS_{Red}$ or $syNOS_{Fl}$ in the absence of Ca^{2+} was
459 used to characterize flavin reduction rates. After purification, $syNOS_{Red}$ contains oxidized FAD
460 and FMN. Attempts to pre-reduce the enzyme to FMNH• with sodium dithionate, DTT and
461 ascorbate caused precipitation without an observable spectral shift to FMNH•. Thus, flavin
462 reduction rates reflect conversion from fully oxidized $syNOS_{Red}$. All stopped flow experiments
463 were carried out anaerobically using a Stopped Flow SX20 instrument (Applied Photophysics).
464 Samples were pre-incubated anaerobically in the presence of the GOD/CAT oxygen scavenging
465 system (see above). Changes in absorbance were detected using a single wavelength
466 Photomultiplier Tube detector. $syNOS_{FL}$ (10 µM) / $syNOS_{Red}$ (40 µM) were mixed with 4x excess
467 NADPH. All data was processed using home-made scripts in R Studio (Posit PBC).

468 **CryoEM grid preparation and data collection - syNOS ligand free**

469 A 4 µl volume of 1.0 mg ml^{-1} syNOS solution, in GFB1, was applied to glow-discharged grids (200
470 mesh Quantifoil Cu, R1.2/1.3; Electron Microscopy Sciences). After 10 s of incubation, the
471 excess solution was blotted for 3.5 s with filter paper by a Vitrobot Mark IV and plunged into
472 liquid ethane, for vitrification (ThermoFisher). CryoEM images of syNOS were collected on a
473 Talos Arctica (ThermoFisher) operated at 200 keV at a nominal magnification of 63,000× with a
474 Gatan GIF Quantum LS Imaging energy filter, using a Gatan K3 direct electron camera in super-
475 resolution counting mode, corresponding to a pixel size of 1.31 Å. A total of 1214 images stacks
476 were obtained with a defocus range of −0.8 to −2.0 µm by Serial EM (University of Colorado-
477 Boulder). Each stack video was recorded for a total dose of 50 electrons per $Å^2$.

478 **CryoEM grid preparation and data collection - turnover conditions**

479 A 4 µl volume of 1.0 mg ml^{-1} syNOS-ligand free solution in GFB1 was applied to glow-discharged
480 grids (200 mesh Quantifoil Cu, R1.2/1.3). After 10s of incubation, the excess solution was
481 blotted for 3.5 s with filter paper by a Vitrobot Mark IV and plunged into liquid ethane for

482 vitrification (ThermoFisher). CryoEM images of syNOS were collected on a Talos Krios
483 (ThermoFisher) operated at 300 keV at a nominal magnification of × 165,000 with a Gatan GIF
484 Quantum LS Imaging energy filter, using a Gatan K3 direct electron CAMera in super-resolution
485 counting mode, corresponding to a pixel size of 0.730 Å. A total of 5001 images stacks were
486 obtained with a defocus rage of −0.6 to −2.0 µm by Leginon (*77*). Each stack video was recorded
487 for a total dose of 44.9 electrons per $Å^2$.

488 **CryoEM grid preparation and data collection - Ca^{2+} and L-arginine conditions**

489 A 4 µl volume of 1.0 mg ml^{-1} syNOS in the presence of 1 mM Ca^{2+} and 1 mM L-arg solution was
490 applied to glow-discharged grids (300 mesh Quantifoil Au, R1.2/1.3). After 10s of incubation, the
491 excess solution was blotted for 2.5 s with filter paper by a Vitrobot Mark IV and plunged into
492 liquid ethane for vitrification (ThermoFisher). CryoEM images of syNOS were collected on a
493 Talos Krios (ThermoFisher) operated at 300 keV at a nominal magnification of 165,000× with a
494 Gatan GIF Quantum LS Imaging energy filter, using a Gatan K3 direct electron camera in super-
495 resolution counting mode, corresponding to a pixel size of 0.422 Å. A total of 5019 images stacks
496 were obtained with a defocus range of −0.6 to −2.0 µm by Leginon (*77*). Each stack video was
497 recorded for a total dose of 50.50 electrons per $Å^2$.

498 **CryoEM Image processing and structural reconstruction**

499 All cryoEM density refinement was performed using CryoSPARC (*50*) as illustrated in Figs. S2-S6.
500 An Alphafold3 prediction was used as the input model by being docked into the appropriate
501 densities using ChimeraX (*50*, *78*, *79*). Ligand and poor fitting regions were built and real space
502 refined using Coot (*79*). The resulting models were passed through ISOLDE (*80*) to approach
503 thermodynamically rational rotamers/conformations. The outputs from these initial models
504 were subjected to a series of real-space refinement using PHENIX (*81*) conformational outlier
505 residues were then adjusted manually using Coot (*79*)

506 **Cytochrome c reduction assay**

507 Cytochrome c (Cc) was used as an electron acceptor to measure the efficiency of electron flow
508 from NOS_{Red}. Cc accepts an electron from the fully reduced $FMNH_2$ and not from $FADH_2$/$FADH^-$

509 $^{\bullet}$/FAD$^{\bullet}$/ FMNH$^{\bullet}$. Cc reduction assays were carried out as previously described (*82*) using an
510 Agilent 8453 UV-Vis Spectrometer with an attached Hewlett Packard 89090A Peltier
511 Temperature Controller for constant temperature at 20 ^{o}C and constant stirring at 400 rpm
512 (Agilent & Hewlett Packard). All reported reactions were carried out in CC buffer (100 mM Tris
513 (pH 7.5) and 200 mM NaCl). Cc was pre-oxidized with 1 mM potassium ferrocyanide and then
514 buffer exchanged into CC buffer. Reactions were conducted with 10 uM Cc and 3 nM of the
515 sample of interest. Reactions were initiated with 1 mM NADPH and were run either in the
516 presence of 1 mM Ca^{2+} or 1 mM EGTA as noted. All data was processed using home-made
517 scripts in R Studio (Posit PBC).

518 **Nitric oxide synthase activity assay**

519 All activity assays were carried out for 30 minutes in 100 mM Tris, (pH 7.5) 200 mM NaCl, 1 mM
520 DTT and 1 mM L-arginine and initiated with 1 mM NADPH (25 °C). Each sample was evaluated in
521 the presence of 1 mM Ca^{2+} or 1 mM EGTA. Post reaction, samples were boiled at 70 ^{o}C to halt
522 NOS activity. NADPH was then precipitated using the $ZnCl_2$/$NaCO_3$ method and subsequently
523 centrifuged at 15000 G at room temperature. The supernatant was then quantified for total
524 NO_2^- and NO_3^- content through the Griess assay as implemented in the Nitrate/Nitrite
525 Colorimetric Assay Kit (Cayman Chemicals).

526 **Oxygen consumption assay to probe Nitric Oxide Dioxygenase activity**

527 The Oxygraph+ system (Hansatech Instruments) was used to measure oxygen consumption of
528 syNOS in the presence of the NO donor, 3-(2-Hydroxy-1-methyl-2-nitrosohydrazino)-N-methyl-1-
529 propanamine (NOC-7). 1 µM of enzyme ($syNOS_{FI}$ or $syNOS_{\Delta C2}$) was incubated in buffer
530 containing 50 mM Tris and 150 mM NaCl at pH 7.5, with 10 µM NOC-7 for 5 minutes. The
531 reaction was initiated with 1 mM NADPH. Three separate controls were performed to rule out
532 superoxide or non-enzymatic NO oxidation: NOC-7 + NADPH, NOC-7 + $syNOS_{FL}$ and syNOS +
533 NADPH.

534

535

536 **Isothermal calorimetry**

537 Thermodynamic binding properties between Ca^{2+} and $syNOS_{C2}$ (1-138) were measured on a
538 Nano ITC Low Volume isothermal titration calorimeter (TA instruments). $SyNOS_{C2}$ was prepared
539 in a 50 mM CHES and 150 mM NaCl buffer at pH 9.0 at 0.072 mM with 200 µL in the sample cell.
540 Lower pHs also gave indication of Ca^{2+} binding, but led to aggregation of the C2 domain that
541 prevented quantitative assessment. $CaCl_2$ was prepared in the same buffer at a concentration of
542 0.250 mM; 2.5uL was titrated every 250 s for a total of 30 injections. Thermal data were
543 analyzed using an independent binding model with the NanoAnalyze software.

544 **Reduction potential determination**

545 Reduction potential measurements were performed using a dye calibration method (*83*, *84*),
546 wherein reduction was driven by a deazaflavin/EDTA photochemical system in a 50 mM $NaPO_3$,
547 10% Glycerol at pH 7.0, with the following modifications: i) 9 µm 5-deazariobflavin and 5 mM
548 EDTA was used as the chemical reductant ii) reactions were equilibrated anaerobically in a coy
549 chamber while supplemented with GOD/CAT oxygen scavenging system. All measurements
550 were carried out using an Agilent 8453 UV-Vis spectrometer with an attached Hewlett Packard
551 89090A Peltier Temperature Controller for maintaining constant temperature at 20 ^{o}C and
552 constant stirring at 400 rpm (Agilent & Hewlett Packard), with the reaction being photoinitiated
553 with a 15 mW 300 nm laser (ThorLabs) placed above the clear septum capping the cuvette.
554 Calibrating dyes per domain were selected based on literature values of the published redox
555 potentials (Table S4). Note that the quoted reduction potentials for $syNOS_{Fld}$ and $syNOS_{FNR}$ will
556 be the average of the single electron couples between semiquinone and oxidized, and
557 hydroquinone and semiquinone.

558

559

560

561

562

563 **References**

564 1. R. M. Palmer, S. Moncada, A novel citrulline-forming enzyme implicated in the formation of nitric
565 oxide by vascular endothelial cells. *Biochem Biophys Res Commun* **158**, 348–352 (1989).

566 2. B. R. Crane, Bacterial Nitric Oxide Synthases. *Annual Review Of Biochemistry* **79** (2010).

567 3. J. A. McCleverty, Chemistry of Nitric Oxide Relevant to Biology. *Chem. Rev.* **104**, 403–418 (2004).

568 4. M. Cossenza, R. Socodato, C. C. Portugal, I. C. L. Domith, L. F. H. Gladulich, T. G. Encarnaçao, K. C.
569 Calaza, H. R. Mendonça, P. Campello-Costa, R. Paes-de-Carvalho, "Nitric Oxide in the Nervous
570 System: Biochemical, Developmental, and Neurobiological Aspects" in *Nitric Oxide*, G. Litwack, Ed.
571 (2014)vol. 96 of *Vitamins and Hormones*, pp. 79–125.

572 5. C. Farah, L. Y. M. Michel, J. L. Balligand, Nitric oxide signalling in cardiovascular health and disease.
573 *Nature Reviews Cardiology* **15**, 292–316 (2018).

574 6. J. O. Lundberg, E. Weitzberg, Nitric oxide signaling in health and disease. *Cell* **185**, 2853–2878
575 (2022).

576 7. M. A. Marletta, Revisiting Nitric Oxide Signaling: Where Was It, and Where Is It Going?
577 *Biochemistry* **60**, 3491–3496 (2021).

578 8. M. Shepherd, D. Giordano, C. Verde, R. K. Poole, The Evolution of Nitric Oxide Function: From
579 Reactivity in the Prebiotic Earth to Examples of Biological Roles and Therapeutic Applications.
580 *Antioxidants* **11** (2022).

581 9. K. A. White, M. A. Marletta, Nitric oxide synthase is a cytochrome P-450 type hemoprotein, *ACS*
582 *Publications* (2002). https://doi.org/10.1021/bi00144a001.

583 10. U. Förstermann, W. C. Sessa, Nitric oxide synthases: regulation and function. *Eur Heart J* **33**, 829–
584 837, 837a–837d (2012).

585 11. M. A. Cinelli, H. T. Do, G. P. Miley, R. B. Silverman, Inducible nitric oxide synthase: Regulation,
586 structure, and inhibition. *Med Res Rev* **40**, 158–189 (2020).

587 12. D. J. Stuehr, M. M. Haque, Nitric oxide synthase enzymology in the 20 years after the Nobel Prize.
588 *British Journal of Pharmacology* **176**, 177–188 (2019).

589 13. J. Reyes-Rivera, Y. Wu, B. G. H. Guthrie, M. A. Marletta, N. King, T. Brunet, Nitric oxide signaling
590 controls collective contractions in a colonial choanoflagellate. *Curr Biol* **32**, 2539-2547.e5 (2022).

591 14. J. Tejero, D. Stuehr, Tetrahydrobiopterin in nitric oxide synthase. *IUBMB Life* **65**, 358–365 (2013).

592 15. D. J. Stuehr, J. Santolini, Z.-Q. Wang, C.-C. Wei, S. Adak, Update on mechanism and catalytic
593 regulation in the NO synthases. *J Biol Chem* **279**, 36167–36170 (2004).

594 16. H. M. Abu-Soud, D. J. Stuehr, Nitric oxide synthases reveal a role for calmodulin in controlling
595 electron transfer. *Proc Natl Acad Sci U S A* **90**, 10769–10772 (1993).

596 17. D. H. Craig, S. K. Chapman, S. Daff, Calmodulin Activates Electron Transfer through Neuronal Nitric-
597 oxide Synthase Reductase Domain by Releasing an NADPH-dependent Conformational Lock *.
598 *Journal of Biological Chemistry* **277**, 33987–33994 (2002).

599 18. N. G. H. Leferink, S. Hay, S. E. J. Rigby, N. S. Scrutton, Towards the free energy landscape for
600 catalysis in mammalian nitric oxide synthases. *The FEBS Journal* **282**, 3016–3029 (2015).

601 19. T. L. Poulos, H. Li, Nitric Oxide Synthase and Structure-Based Inhibitor Design. *Nitric Oxide* **63**, 68–
602 77 (2017).

603 20. L. Zhou, D.-Y. Zhu, Neuronal nitric oxide synthase: Structure, subcellular localization, regulation, and
604 clinical implications. *Nitric Oxide* **20**, 223–230 (2009).

605 21. V. Garcia, W. C. Sessa, Endothelial NOS: perspective and recent developments. *Br J Pharmacol* **176**,
606 189–196 (2019).

607 22. N. A. Popova, S. K. Soodaeva, I. A. Klimanov, V. M. Misharin, A. A. Temnov, Autoregulation and
608 Autoinhibition of the Main NO Synthase Isoforms (Brief Review). *Sovremennye Tehnologii V*
609 *Medicine* **15**, 53–59 (2023).

610 23. M. C. Surdel, B. F. Dutter, G. A. Sulikowski, E. P. Skaar, Bacterial Nitric Oxide Synthase Is Required for
611 the Staphylococcus aureus Response to Heme Stress. *ACS Infect. Dis.* **2**, 572–578 (2016).

612 24. I. Gusarov, K. Shatalin, M. Starodubtseva, E. Nudler, Endogenous Nitric Oxide Protects Bacteria
613 Against a Wide Spectrum of Antibiotics. *Science* **325**, 1380–1384 (2009).

614 25. B. A. Patel, M. Moreau, J. Widom, H. Chen, L. Yin, Y. Hua, B. R. Crane, Endogenous nitric oxide
615 regulates the recovery of the radiation-resistant bacterium Deinococcus radiodurans from
616 exposure to UV light. *Proc Natl Acad Sci U S A* **106**, 18183–18188 (2009).

617 26. N. Gupta, A. Srivastava, A. K. Mishra, Nitric Oxide Synthases in Cyanobacteria: Diversity, Cellular
618 Implications and Ecological Pertinence. *J Plant Growth Regul* **44**, 508–528 (2025).

619 27. T. G. Popova, A. Teunis, H. Vaseghi, W. Zhou, V. Espina, L. A. Liotta, S. G. Popov, Nitric oxide as a
620 regulator of *B-anthracis* pathogenicity. *Frontiers in Microbiology* **6** (2015).

621 28. P. R. Gardner, Nitric oxide dioxygenase function and mechanism of flavohemoglobin, hemoglobin,
622 myoglobin and their associated reductases. *J Inorg Biochem* **99**, 247–266 (2005).

623 29. P. R. Gardner, A. M. Gardner, L. A. Martin, A. L. Salzman, Nitric oxide dioxygenase: An enzymic
624 function for flavohemoglobin. *Proceedings of the National Academy of Sciences* **95**, 10378–10383
625 (1998).

626 30. M. E. S. Lewis, H. A. Corker, B. Gollan, R. K. Poole, “A survey of methods for the purification of
627 microbial flavohemoglobins” in *Globins and Other Nitric Oxide-Reactive Proteins, Pt A*, R. K. Poole,
628 Ed. (2008)vol. 436 of *Methods in Enzymology*, pp. 169–186.

31. F. Del Castello, N. Foresi, A. Nejamkin, C. Lindermayr, F. Buegger, L. Lamattina, N. Correa-Aragunde, Cyanobacterial NOS expression improves nitrogen use efficiency, nitrogen-deficiency tolerance and yield in Arabidopsis. *Plant Science* **307** (2021).

32. N. Correa-Aragunde, N. Foresi, F. Del Castello, L. Lamattina, A singular nitric oxide synthase with a globin domain found in Synechococcus PCC 7335 mobilizes N from arginine to nitrate. *Sci Rep* **8**, 12505 (2018).

33. M. M. Labarthe, G. A. Maroniche, L. Lamattina, C. M. Creus, Nitric oxide synthase expression in Pseudomonas koreensis MME3 improves plant growth promotion traits. *Appl. Microbiol. Biotechnol.* **108** (2024).

34. A. L. Picciano, B. R. Crane, A nitric oxide synthase-like protein from Synechococcus produces NO/NO3- from l-arginine and NADPH in a tetrahydrobiopterin- and Ca2+-dependent manner. *J Biol Chem* **294**, 10708–10719 (`).

35. M. G. Campbell, B. C. Smith, C. S. Potter, B. Carragher, M. A. Marletta, Molecular architecture of mammalian nitric oxide synthases. *Proc Natl Acad Sci U S A* **111**, E3614-3623 (2014).

36. D. Felker, K. Lee, T. H. Pospiech, Y. Morishima, H. Zhang, M. Lau, D. R. Southworth, Y. Osawa, Mapping interactions of calmodulin and neuronal NO synthase by crosslinking and mass spectrometry. *Journal of Biological Chemistry* **300** (2024).

37. A. L. Yokom, Y. Morishima, M. Lau, M. Su, A. Glukhova, Y. Osawa, D. R. Southworth, Architecture of the nitric-oxide synthase holoenzyme reveals large conformational changes and a calmodulin-driven release of the FMN domain. *J Biol Chem* **289**, 16855–16865 (2014).

38. B. C. Smith, E. S. Underbakke, D. W. Kulp, W. R. Schief, M. A. Marletta, Nitric oxide synthase domain interfaces regulate electron transfer and calmodulin activation. *Proc Natl Acad Sci U S A* **110**, E3577-3586 (2013).

39. T. Jiang, M. C. Thielges, C. J. Feng, Emerging approaches to investigating functional protein dynamics in modular redox enzymes: Nitric oxide synthase as a model system. *J. Biol. Chem.* **301** (2025).

40. C. R. Pudney, D. J. Heyes, B. Khara, S. Hay, S. E. J. Rigby, N. S. Scrutton, Kinetic and spectroscopic probes of motions and catalysis in the cytochrome P450 reductase family of enzymes. *Febs Journal* **279**, 1534–1544 (2012).

41. T. M. Hedison, N. G. H. Leferink, S. Hay, N. S. Scrutton, Correlating Calmodulin Landscapes with Chemical Catalysis in Neuronal Nitric Oxide Synthase using Time-Resolved FRET and a 5-Deazaflavin Thermodynamic Trap. *Acs Catalysis* **6**, 5170–5180 (2016).

42. T. M. Hedison, S. Hay, N. S. Scrutton, Trapping methods for probing functional intermediates in nitric oxide synthases and related enzymes. *Frontiers in Bioscience-Landmark* **23**, 1874–1888 (2018).

43. Y. He, M. M. Haque, D. J. Stuehr, H. P. Lu, Conformational states and fluctuations in endothelial nitric oxide synthase under calmodulin regulation. *Biophysical Journal* **120**, 5196–5206 (2021).

44. J. Li, H. Zheng, C. Feng, Deciphering mechanism of conformationally controlled electron transfer in nitric oxide synthases. *Frontiers in Bioscience-Landmark* **23**, 1803–1821 (2018).

45. C. J. Feng, Mechanism of nitric oxide synthase regulation: Electron transfer and interdomain interactions. *Coordination Chemistry Reviews* **256**, 393–411 (2012).

46. D. J. Stuehr, J. Tejero, M. M. Haque, Structural and mechanistic aspects of flavoproteins: electron transfer through the nitric oxide synthase flavoprotein domain. *The FEBS Journal* **276**, 3959–3974 (2009).

47. M. M. Haque, C. Kenney, J. Tejero, D. J. Stuehr, A kinetic model linking protein conformational motions, interflavin electron transfer and electron flux through a dual-flavin enzyme-simulating the reductase activity of the endothelial and neuronal nitric oxide synthase flavoprotein domains. *FEBS J* **278**, 4055–69 (Nov).

48. R. Chakravarti, K. S. Aulak, P. L. Fox, D. J. Stuehr, GAPDH regulates cellular heme insertion into inducible nitric oxide synthase. *Proceedings of the National Academy of Sciences* **107**, 18004–18009 (2010).

49. Y. Morishima, M. Lau, W. B. Pratt, Y. Osawa, Dynamic cycling with a unique Hsp90/Hsp70-dependent chaperone machinery and GAPDH is needed for heme insertion and activation of neuronal NO synthase. *J Biol Chem* **299**, 102856 (2023).

50. A. Punjani, J. L. Rubinstein, D. J. Fleet, M. A. Brubaker, cryoSPARC: algorithms for rapid unsupervised cryo-EM structure determination. *Nat Methods* **14**, 290–296 (2017).

51. T. Wagner, F. Merino, M. Stabrin, T. Moriya, C. Antoni, A. Apelbaum, P. Hagel, O. Sitsel, T. Raisch, D. Prumbaum, D. Quentin, D. Roderer, S. Tacke, B. Siebolds, E. Schubert, T. R. Shaikh, P. Lill, C. Gatsogiannis, S. Raunser, SPHIRE-crYOLO is a fast and accurate fully automated particle picker for cryo-EM. *Commun Biol* **2**, 218 (2019).

52. B. R. Crane, The enzymology of nitric oxide in bacterial pathogenesis and resistance. *Biochemical Society Transactions* **36**, 1149–1154 (2008).

53. K. Pant, A. M. Bilwes, S. Adak, D. J. Stuehr, B. R. Crane, Structure of a nitric oxide synthase heme protein from Bacillus subtilis. *Biochemistry* **41**, 11071–9 (2002).

54. B. R. Crane, A. S. Arvai, D. K. Ghosh, C. Wu, E. D. Getzoff, D. J. Stuehr, J. A. Tainer, Structure of nitric oxide synthase oxygenase dimer with pterin and substrate. *Science* **279**, 2121–6 (1998).

55. S. Corbalan-Garcia, J. C. Gómez-Fernández, Signaling through C2 domains: More than one lipid target. *Biochimica et Biophysica Acta (BBA) - Biomembranes* **1838**, 1536–1547 (2014).

56. T. A. Leonard, "C2 Domain Proteins" in *Encyclopedia of Metalloproteins*, R. H. Kretsinger, V. N. Uversky, E. A. Permyakov, Eds. (Springer, New York, NY, 2013; https://doi.org/10.1007/978-1-4614-1533-6_39), pp. 309–318.

57. U. Siddhanta, A. Presta, B. Fan, D. Wolan, D. L. Rousseau, D. J. Stuehr, Domain Swapping in Inducible Nitric-oxide Synthase: ELECTRON TRANSFER OCCURS BETWEEN FLAVIN AND HEME

GROUPS LOCATED ON ADJACENT SUBUNITS IN THE DIMER*. *Journal of Biological Chemistry* **273**, 18950–18958 (1998).

58. J. Tejero, M. M. Haque, D. Durra, D. J. Stuehr, A Bridging Interaction Allows Calmodulin to Activate NO Synthase through a Bi-modal Mechanism. *J Biol Chem* **285**, 25941–25949 (2010).

59. P.-F. Chen, K. K. Wu, Structural elements contribute to the calcium/calmodulin dependence on enzyme activation in human endothelial nitric-oxide synthase. *J Biol Chem* **278**, 52392–52400 (2003).

60. E. D. Garcin, C. M. Bruns, S. J. Lloyd, D. J. Hosfield, M. Tiso, R. Gachhui, D. J. Stuehr, J. A. Tainer, E. D. Getzoff, Structural Basis for Isozyme-specific Regulation of Electron Transfer in Nitric-oxide Synthase * [boxs]. *Journal of Biological Chemistry* **279**, 37918–37927 (2004).

61. B. Ghazi Esfahani, N. Walia, K. Neselu, Y. Garg, M. Aragon, I. Askenasy, H. A. Wei, J. H. Mendez, M. E. Stroupe, Structure of dimerized assimilatory NADPH-dependent sulfite reductase reveals the minimal interface for diflavin reductase binding. *Nat Commun* **16**, 2955 (2025).

62. H. Olteanu, R. Banerjee, Human Methionine Synthase Reductase, a Soluble P-450 Reductase-like Dual Flavoprotein, Is Sufficient for NADPH-dependent Methionine Synthase Activation *. *Journal of Biological Chemistry* **276**, 35558–35563 (2001).

63. Z.-Q. Wang, R. J. Lawson, M. R. Buddha, C.-C. Wei, B. R. Crane, A. W. Munro, D. J. Stuehr, Bacterial flavodoxins support nitric oxide production by Bacillus subtilis nitric-oxide synthase. *J Biol Chem* **282**, 2196–2202 (2007).

64. S. Daff, I. Sagami, T. Shimizu, The 42-amino acid insert in the FMN domain of neuronal nitric-oxide synthase exerts control over Ca(2+)/calmodulin-dependent electron transfer. *J Biol Chem* **274**, 30589–30595 (1999).

65. M. Tiso, J. Tejero, K. Panda, K. S. Aulak, D. J. Stuehr, Versatile regulation of neuronal nitric oxide synthase by specific regions of its C-terminal tail. *Biochemistry* **46**, 14418–28 (2007).

66. L. J. Roman, R. T. Miller, M. A. de La Garza, J. J. Kim, B. S. Siler Masters, The C terminus of mouse macrophage inducible nitric-oxide synthase attenuates electron flow through the flavin domain. *J Biol Chem* **275**, 21914–21919 (2000).

67. L. J. Roman, P. Martásek, R. T. Miller, D. E. Harris, M. A. de La Garza, T. M. Shea, J. J. Kim, B. S. Masters, The C termini of constitutive nitric-oxide synthases control electron flow through the flavin and heme domains and affect modulation by calmodulin. *J Biol Chem* **275**, 29225–29232 (2000).

68. D. Hamdane, C. Xia, S.-C. Im, H. Zhang, J.-J. P. Kim, L. Waskell, Structure and Function of an NADPH-Cytochrome P450 Oxidoreductase in an Open Conformation Capable of Reducing Cytochrome P450*. *Journal of Biological Chemistry* **284**, 11374–11384 (2009).

69. M. Tiso, D. W. Konas, K. Panda, E. D. Garcin, M. Sharma, E. D. Getzoff, D. J. Stuehr, C-terminal Tail Residue Arg1400 Enables NADPH to Regulate Electron Transfer in Neuronal Nitric-oxide Synthase *. *Journal of Biological Chemistry* **280**, 39208–39219 (2005).

739 70. S. Adak, M. Sharma, A. L. Meade, D. J. Stuehr, A conserved flavin-shielding residue regulates NO
740 synthase electron transfer and nicotinamide coenzyme specificity. *Proceedings of the National*
741 *Academy of Sciences* **99**, 13516–13521 (2002).

742 71. E. A. Nalefski, J. J. Falke, The C2 domain calcium-binding motif: structural and functional diversity.
743 *Protein Sci* **5**, 2375–2390 (1996).

744 72. N. Verdaguer, S. Corbalan-Garcia, W. F. Ochoa, I. Fita, J. C. Gómez-Fernández, Ca2+ bridges the C2
745 membrane-binding domain of protein kinase Cα directly to phosphatidylserine. *The EMBO Journal*
746 **18**, 6329–6338 (1999).

747 73. L. Zheng, R. Krishnamoorthi, M. Zolkiewski, X. Wang, Distinct Ca2+ Binding Properties of Novel C2
748 Domains of Plant Phospholipase Dα and β *. *Journal of Biological Chemistry* **275**, 19700–19706
749 (2000).

750 74. C. C. Moser, J. M. Keske, K. Warncke, R. S. Farid, P. L. Dutton, Nature of biological electron transfer.
751 *Nature* **355**, 796–802 (1992).

752 75. J. B. Hopkins, R. E. Gillilan, S. Skou, BioXTAS RAW: improvements to a free open-source program for
753 small-angle X-ray scattering data reduction and analysis. *J Appl Cryst* **50**, 1545–1553 (2017).

754 76. C. E. Aitken, R. A. Marshall, J. D. Puglisi, An Oxygen Scavenging System for Improvement of Dye
755 Stability in Single-Molecule Fluorescence Experiments. *Biophys J* **94**, 1826–1835 (2008).

756 77. A. Cheng, C. Negro, J. F. Bruhn, W. J. Rice, S. Dallakyan, E. T. Eng, D. G. Waterman, C. S. Potter, B.
757 Carragher, Leginon: New features and applications. *Protein Sci* **30**, 136–150 (2021).

758 78. J. Abramson, J. Adler, J. Dunger, R. Evans, T. Green, A. Pritzel, O. Ronneberger, L. Willmore, A. J.
759 Ballard, J. Bambrick, S. W. Bodenstein, D. A. Evans, C.-C. Hung, M. O'Neill, D. Reiman, K.
760 Tunyasuvunakool, Z. Wu, A. Žemgulytė, E. Arvaniti, C. Beattie, O. Bertolli, A. Bridgland, A.
761 Cherepanov, M. Congreve, A. I. Cowen-Rivers, A. Cowie, M. Figurnov, F. B. Fuchs, H. Gladman, R.
762 Jain, Y. A. Khan, C. M. R. Low, K. Perlin, A. Potapenko, P. Savy, S. Singh, A. Stecula, A.
763 Thillaisundaram, C. Tong, S. Yakneen, E. D. Zhong, M. Zielinski, A. Žídek, V. Bapst, P. Kohli, M.
764 Jaderberg, D. Hassabis, J. M. Jumper, Accurate structure prediction of biomolecular interactions
765 with AlphaFold 3. *Nature* **630**, 493–500 (2024).

766 79. P. Emsley, K. Cowtan, Coot: model-building tools for molecular graphics. *Acta Crystallogr D Biol*
767 *Crystallogr* **60**, 2126–32 (2004).

768 80. T. I. Croll, ISOLDE: a physically realistic environment for model building into low-resolution electron-
769 density maps. *Acta Cryst D* **74**, 519–530 (2018).

770 81. (IUCr) Real-space refinement in PHENIX for cryo-EM and crystallography.
771 https://journals.iucr.org/d/issues/2018/06/00/ic5103/index.html.

772 82. F. P. Guengerich, M. V. Martin, C. D. Sohl, Q. Cheng, Measurement of cytochrome P450 and
773 NADPH–cytochrome P450 reductase. *Nat Protoc* **4**, 10.1038/nprot.2009.121 (2009).

83. Z. A. Maschmann, T. K. Chua, S. Chandrasekaran, H. Ibáñez, B. R. Crane, Redox properties and PAS domain structure of the Escherichia coli energy sensor Aer indicate a multistate sensing mechanism. *J Biol Chem* **298**, 102598 (2022).

84. S. L. Christgen, S. M. Becker, D. F. Becker, Methods for determining the reduction potentials of flavin enzymes. *Methods Enzymol* **620**, 1–25 (2019).

Acknowledgements: We thank Angela Picciano for helpful discussions. We thank the National Center for CryoEM Access and Training (NCCAT) and the Cornell Center for Material Science (CCMR) for access to data collection facilities. We thank Yajie Xu and Dr Mariena Silvestry Ramos for assistance in CryoEM training and data collection.

Funding: This work was supported by grant MCB-2129728 from the National Science Foundation to BRC. **Author contributions:** D.N. and B.R.C. designed research, conducted research, analyzed data and wrote the manuscript. Competing interests: The authors declare that they have no competing interests. Data and materials availability: The cryoEM data and structures are available at the Protein Data Bank with accession codes: 9Q05, 9Q06, 9Q0Y, 9Q0X, and 9Q15. All other data needed to evaluate the conclusions in the paper are present in the paper or the Supplementary Materials.

801 **Figures**

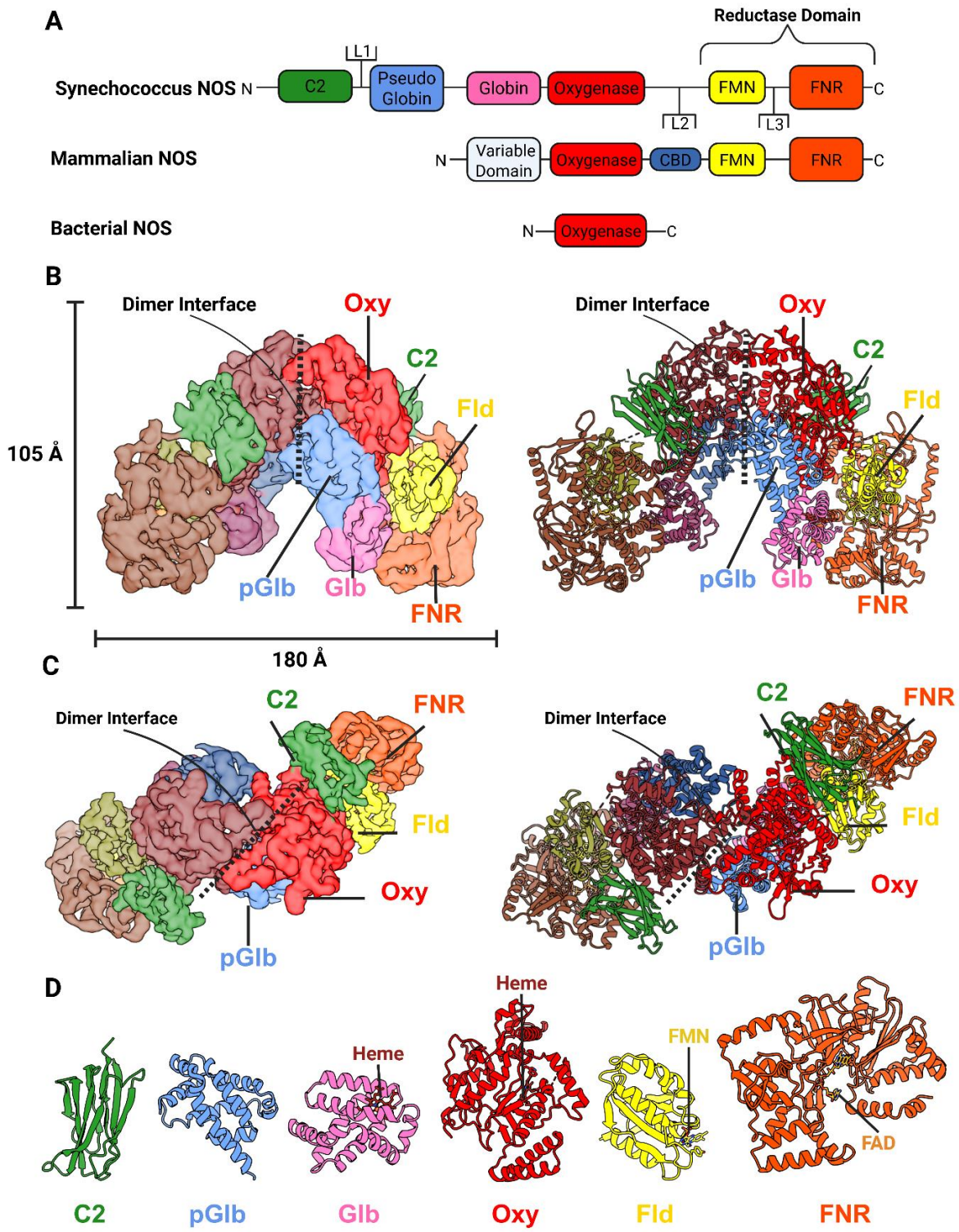

802

803 **Figure 1.** Architecture of Ca^{2+}-free locked syNOS (A) Gene architecture of Synechococcus NOS,
804 mammalian NOS and a typical bacterial NOS. Note that some non-cyanobacterial prokaryotic
805 NOSs have auxiliary domains. (B) Sideview of electron density (left, threshold = 0.0298, C2
806 symmetry applied) and corresponding ribbon representation (right) for the locked syNOS
807 homodimer (NOS-Sym). Domains colored as designated with the two subunits distinguished by
808 the degree of shading. (C) Top view of (B). (D) Individual syNOS domains with cofactors
809 indicated.

810

811

812

813

814

815

816

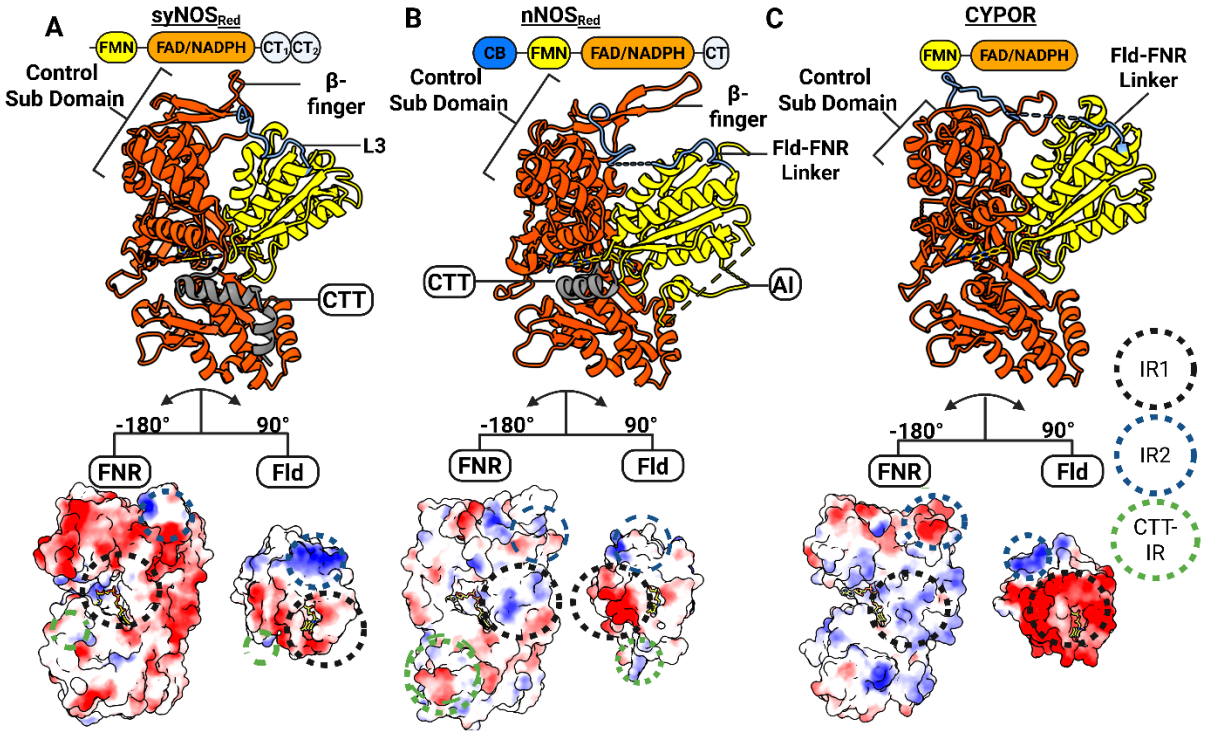

Figure 2. Structural comparison of syNOS$_{Red}$, nNOS$_{Red}$, and CYPOR (A-C). Domain architectures (top), the corresponding ribbon diagrams (middle), and key interfaces (lower) mediated by electrostatic interactions for syNOS$_{Red}$ (A), nNOS$_{Red}$ (PDB:1TLL, B) and CYPOR (PDB:1AMO, C) Surfaces are colored by coulombic electrostatic potential (blue – positive; white – neutral; red – negative)) with the Fld and FNR domains separated and rotated to view the interface. Interfacing Regions (IR) 1 (basic-to-acidic patch interactions between the FAD and FMN binding pockets), IR2 (Fld interaction-to-FNR-control region) and CTT-IR (CTT interaction with Fld) are denoted by colored circles.

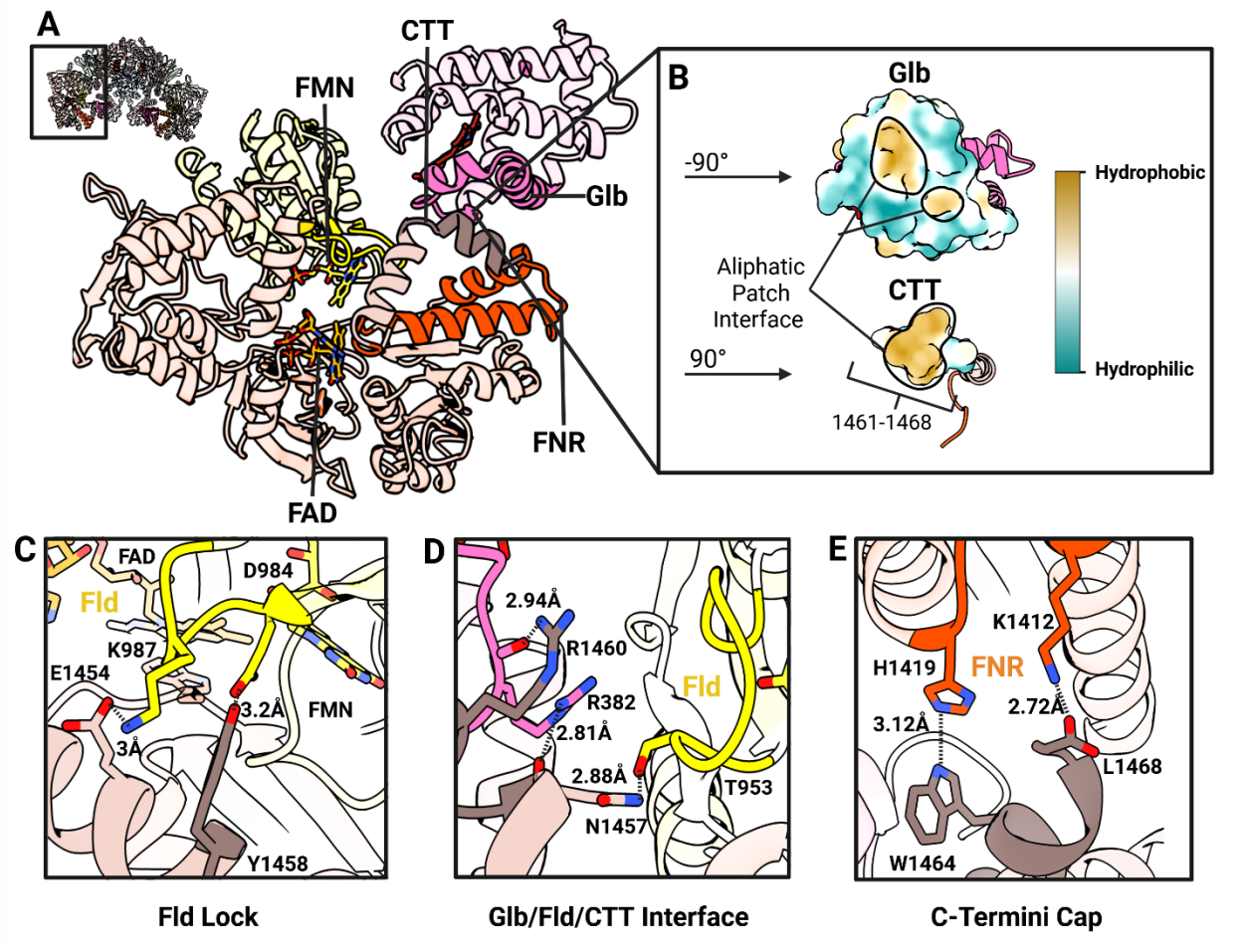

Figure 3. CTT interactions that stabilize the NOS_{Red}-NOS_{Glb} locked state. (A) Ribbon diagram of $syNOS_{Red}$ and $syNOS_{Glb}$ from the boxed region of inactivated $syNOS_{FL}$ (upper left inset) showing key stabilizing interfaces. (B) Aliphatic surface patch between $syNOS_{CTT}$ and $syNOS_{Glb}$ shown by hydrophobicity (yellow) after separating and rotating each domain to view the interface. (C) Fld-to-CTT lock interface mediated by Lys987(Fld)/Glu1454(CTT) salt bridge and Asp984(Fld)/Tyr1458(FNR) hydrogen bond. (D) Fld-to-Glb interface mediated by Asn1457(CTT)/Thr953(Fld) hydrogen bond, Arg1460(CTT)/Arg382-carbonyl(Glb) hydrogen bond and Asn1457-carbonyl(CTT)/arg382(Glb) hydrogen bond. (E) C-Terminal cap interface mediated by Trp1419(CTT)/His1419(FNR) hydrogen bond and a Leu1468-Carboxyl(CTT)/Lys1412 salt bridge.

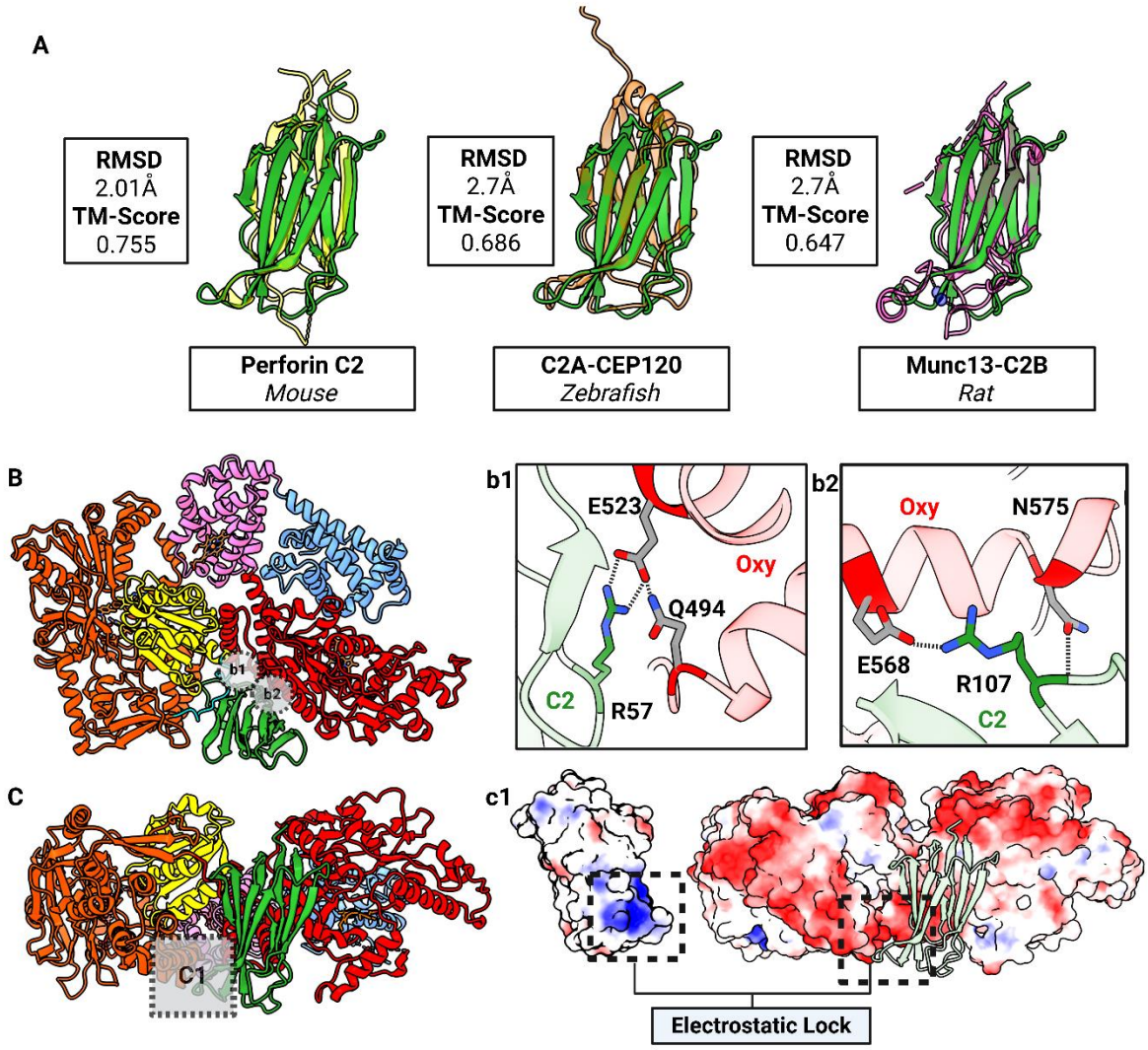

Figure 4. syNOS$_{C2}$ interactions with NOS$_{FNR}$ and NOS$_{Oxy}$. (A) Superimposition of syNOS (C2, green) with Perforin C2 (PDB: 4Y1S, yellow), C2A-CEP120 (PDB:6EWL, orange) and Munc13-C2B (PDB:6NYT, magenta) as labeled, with root mean square deviation (RMSD) of Cα positions (RMSD), and Template Modeling (TM) scores boxed. B) Ribbon diagram of a syNOS subunit, colored by domain with key C2-Oxy interactions shown in insets b1 and b2. b1) Salt bridge between Arg57(C2)/Glu523(Oxy) with Glu523 stabilized by Gln494. b2) Salt bridge between Arg107(C2)/Glu568(Oxy) with the Arg107 amide stabilized by Asn575. (C) Ribbon diagram of a syNOS subunit showing the electrostatic lock interface between syNOS$_{C2}$ and syNOS$_{Oxy}$ in box inset c1. (c1) C2 rotated 90° (left) and FNR (right, orientation as in (C), colored by electrostatic

surfaces (colored: blue-positive, white-intermediate and red –negative). C2 (green, ribbons) is also shown in its original position for reference.

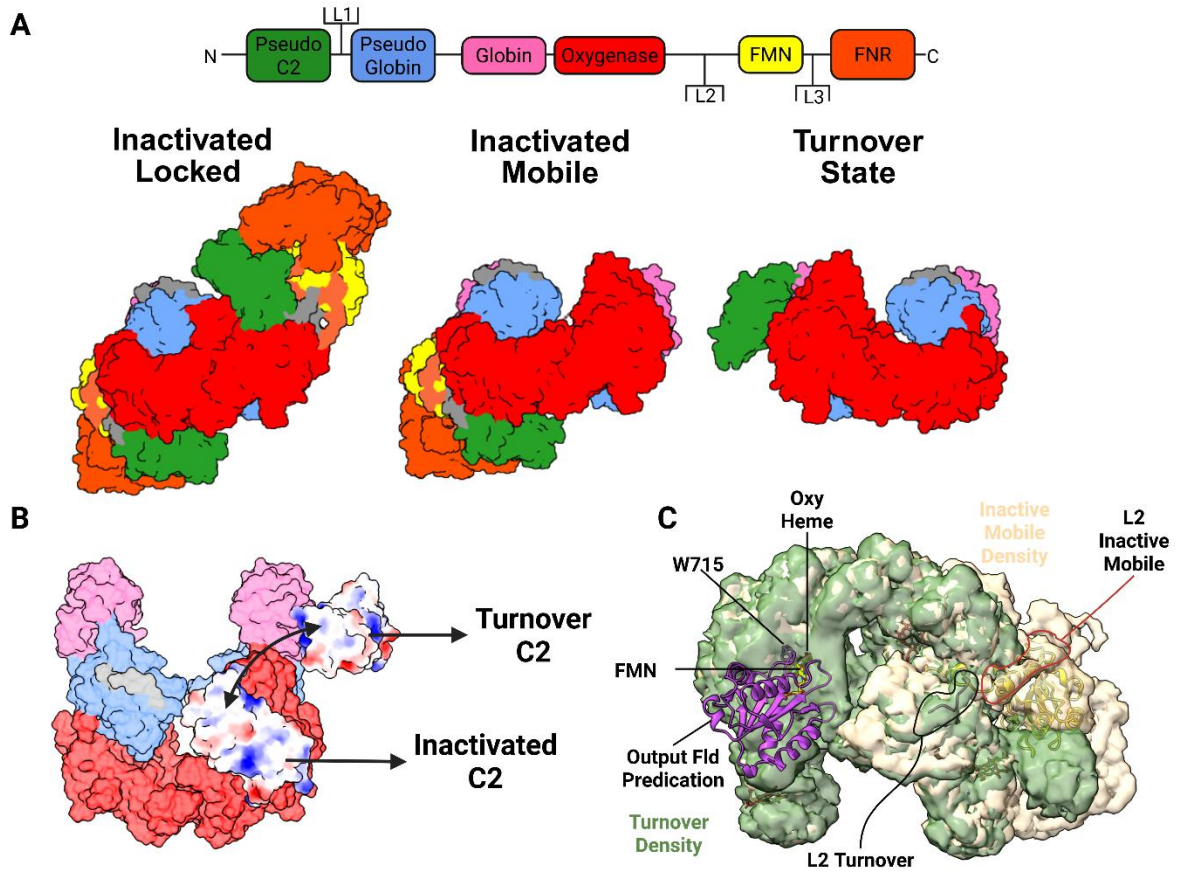

Figure 5. Ca^{2+}-activated C2 mobility. (A) syNOS gene architecture colored by domain, with linkers labeled L1-3(above). Surface representation of three separate syNOS states with relative orientations of the C2 domain. (B) Superimposed surface representations of the turnover state and inactivated states reveal dramatically different C2 positions. (C) L2 in the turnover state (tan electron density) connects to the Fld (yellow ribbons) but then swivels 135° (green density) from its position in the inactivated state to direct the NOS_{Fld} to the adjacent NOS_{Oxy} subunit (purple ribbons of AlphaFold prediction).

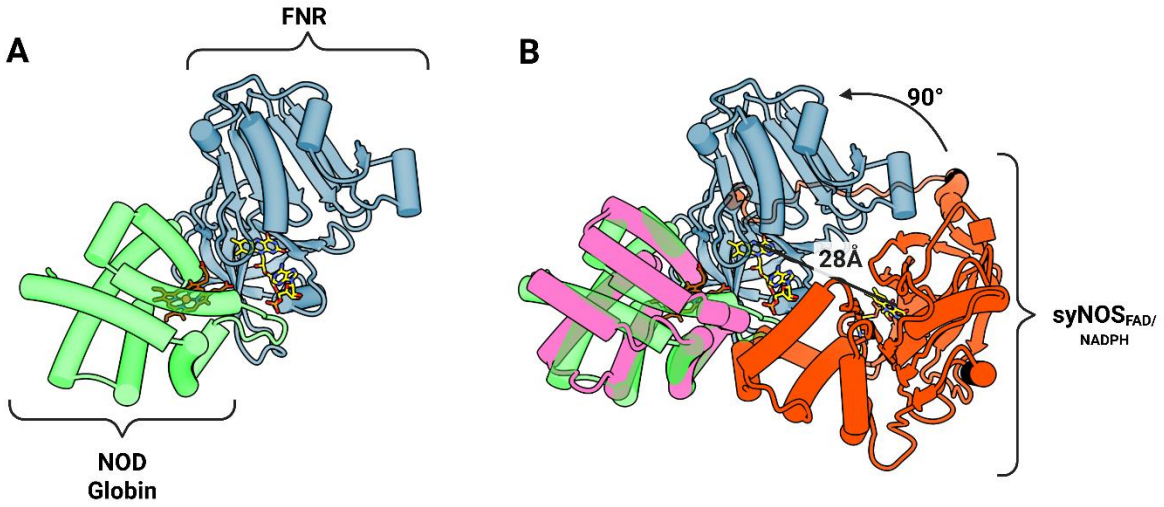

867

868 **Figure 6.** syNOS$_{FNR}$ requires a large conformational change to reduce syNOS$_{Glb}$. (A) Cartoon
869 representation of E.*coli* Hmp (PDB: 1GVH) with the NOD domain (lime green) and FNR (metallic
870 blue) domains orientated to show the Heme-to-FAD separation of 17.8 Å. (B) syNOS$_{Glb}$ (purple)
871 and associated syNOS$_{FNR}$ domain (red, control region 1084-1224 not shown) superimposed on
872 the Hmp Glb (green) and associated FNR (blue). SyNOS$_{FNR}$ would need to rotate 90° and
873 translate 28 Å to adopt an equivalent Hmp conformation.

874

875

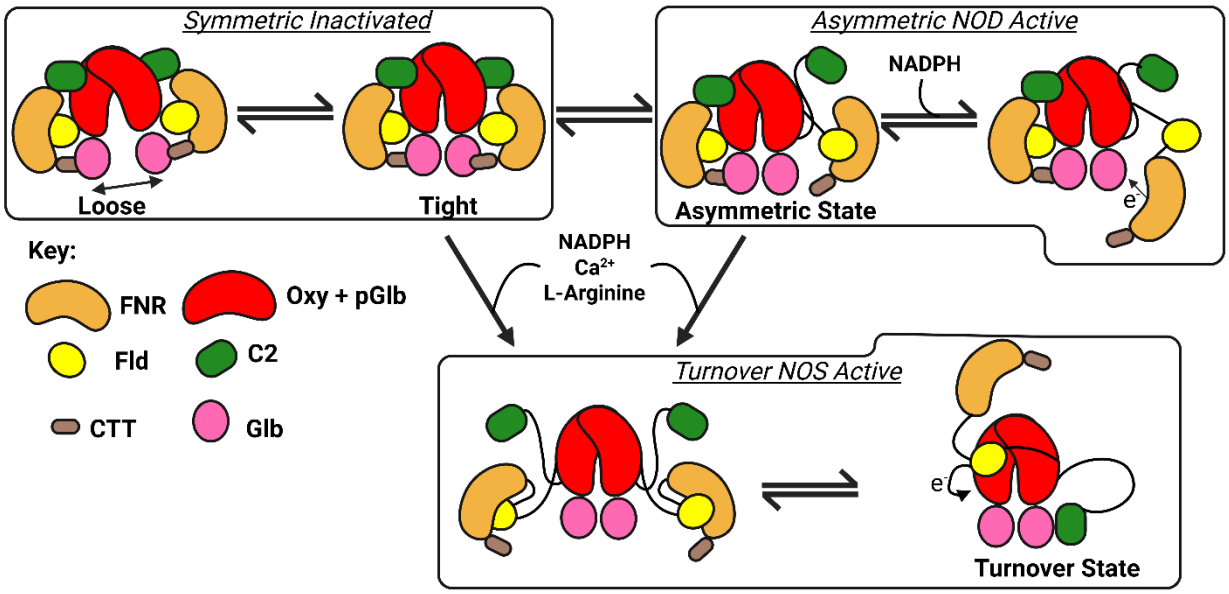

Figure 7. Model for NOS to NOD activity switching in syNOS. In the inactivated locked state $syNOS_{Oxy}$ equilibrates between a loose and tight dimer, the latter stabilized by BH_4. This state can transition into the asymmetric NOD active state which involves a release of a C2 domain from one subunit and increased mobility of NOS_{Fld} and NOS_{FNR}, such that NOS_{FNR} can reduce the $syNOS_{Glb}$ to activate NOD activity. $SyNOS_{Glb}$ reduction coincides with a loosening of the CTT to allow hydride transfer from NADPH to FAD and movement of $syNOS_{FNR}$. In the presence of Ca^{2+}/NADPH/L-arginine syNOS rearranges to facilitate NOS activity. The displacement of NOS_{C2} from NOS_{Oxy} and its binding to NOS_{Glb} relieves constraints on L2 and exposes the Trp715 site such that NOS_{FNR} can relocate to NOSOxy on the opposing subunit and reduce the NOS_{Oxy} heme for NO production.

Structure and dynamics of a muti-domain nitric oxide synthase regulated by a C2 domain

Dhruva Nair and Brian R. Crane

Supplementary Movies

Movie S1: 3D Flexible Refinement of syNOS dimer shows a 'breathing' motion

Supplementary Tables

Table S1: Description of datasets, conditions and refined classes.

Table S2: Cryo-EM data collection, refinement, and validation statistics.

Table S3: DNA primers used in the study with the cloning approach.

Table S4: Reduction potentials ($E^{0'}$) for $syNOS_{Glb}$, $syNOS_{Fld}$ and $syNOS_{FNR}$ vs. the Normal Hydrogen Electrode (NHE)

Supplementary Figures

Figure S1: syNOS purification

Figure S2: Dataset 1 processing scheme

Figure S3: Dataset 2 processing scheme

Figure S4: Merged data for NOS-Sym state, boxed class used for 3DVA and 3DFlex

Figure S5: Dataset 3 processing scheme and validation.

Figure S6: Dataset 4 processing scheme and validation

Figure S7: Dataset 5 processing scheme and validation.

Figure S8: syNOS linker intertwining.

Figure S9: syNOS tight and loose NOS_{Oxy} states.

Figure S10: Phylogenetic sequence clustering in the context of syNOS (residues 853-1468).

Figure S11: C-terminal tail (CTT) sequence alignment of syNOS, mNOSs and diatom NOS.

Figure S12: SEC-SAXS of syNOS and variants.

Figure S13: Steady state cytochrome c reductase activities of WT syNOS and variants expressed as turnover numbers (Cc reduced (NOS subunit)$^{-1}$).

Figure S14: Flavin reduction by NADPH.

Figure S15: Isothermal calorimetric titration of Ca^{2+} with $syNOS_{C2}$ (residues 1-138).

Figure S16: syNOS NOD activity and heme reduction rates

Figure S17: Output state predicted by AlphaFold3.

Supplemental Movies

Movie S1. 3D Variability analysis of one subunit of the syNOS asymmetric dimer showing the breathing motion of NOS_{Red} as a unit relative to motion about the NOS_{Oxy} interface.

Supplementary Tables

Dataset	Conditions	Class 1	Class 2
1 **2**	Heme/FAD/FMN	Symmetric Dimer (NOS-Sym)	Asymmetric Dimer (NOS-Asym)
3	Ca^{2+}/L-arg/BH_4	Asymmetric Dimer (NOS-Asym)	Turnover (NOS-TO_L)
4	Ca^{2+}/L-arg/BH_4	Asymmetric Dimer (NOS-Asym)	Turnover (NOS-TO_T)
5	Ca^{2+}/L-arg/ BH_4/NADPH	Monomer (NOS-Mon)	none

Table S1. Description of datasets, conditions and refined classes.

Dataset		Ca2+/L-Arginine			Ca^{2+}/L-Arginine/NADPH
State	**Symmetric Dimer**	**Asymmetric**	**Turnover**	**Asymmetric (Composite)**	**Monomer**
Data Collection and Processing					
Microscope	Arctica		Krios		Krios
Voltage (keV)	200		300		300
Detector	K3		Gatan K3		Falcon4EC
Nominal magnification	63,000		105,000		105,000
Data Acquisition Software	Serial EM		Leginon		Leginon
Electron dose (e–/Å2)	50		50.5		44.95
Pixel Size (Å) (binned)	1.31		0.422(0.844)		0.7304
Defocus range (μm)	0.5-2		0.4-2.1		0.4-2.2
Number of movies (#)	1214 + 4055		5019		9036
Number of particles	131,000	70,944	61,553	70,944	45,964
Symmetry imposed	C2	C1	C1	C1	C1
Resolution (Å)	3.95	3.16	3.69	3.16	3.09
FSC threshold	0.143	0.143	0.143	0.143	0.143
Refinement					
Initial model used	PDB 9Q15	PDB 9Q15	PDB 9Q15	Alphafold	PDB 9Q15
Non-hydrogen atoms	22712	16319	11268	16319	11404
Protein residues	2796	2001	1358	2001	1398
Ligand(#)	Heme(4) FAD(2) FMN(2)	Heme(2) FAD(1) FMN(1)	Heme(4)	Heme(4) FAD(1) FMN(1)	Heme(2) FAD(1) FMN(1) NADPH(1)
RMS Deviation					
Bond lengths (Å)	0.02	0.005	0.003	0.003	0.003
Bond angles (°)	1.55	0.55	0.574	0.485	0.519
MolProbity score	1.54	1.58	1.5	1.74	1.54
Clashscore	2.18	3.49	4.65	4.66	4.93
Poor rotamers (%)	2.08	1.63	0.93	1.8	0.91
Ramachandran Favored (%)	95.1	96.0	96.1	95.5	96.0
Ramachandran Allowed (%)	4.6	3.9	3.7	4.3	3.8
Ramachandran Disallowed (%)	0.3	0.2	0.2	0.2	0.2
Fit to map (CCmask)	0.8	0.79	0.75	0.81	0.82
EMDB (maps)	EMD-72088	EMD-72110	EMD-72109	EMD-72104, EMD-72105,EMD-72116	EMD-72087
PDB (model)	9Q06	9Q0Y	9Q0X	9Q15	9Q05

Table S2. Cryo-EM data collection, refinement, and validation statistics.

Primer Name	Primer	Cloning Approach
pet28_twin_strep_syNOS_fwd	tcgagcaccaccaccacc	Gibson/NEB HiFi
pet28_twin_strep_syNOS_rev	catatgtcctccggattggaagtac	Gibson/NEB HiFi
syNOS_fwd	tccaatccggaggacatatgatgcttgtcaacgactctc	Gibson/NEB HiFi
syNOS_rev	gtggtggtggtggtgctcgagctacaagttggctagcc	Gibson/NEB HiFi
Hptg_fwd_PAYC_mcs1	TAATGCTTAAGTCGAACAG	Gibson/NEB HiFi
Hptg_rev_PAYC_mcs1	GGTATATCTCCTTATTAAAGTTAAAC	Gibson/NEB HiFi
Hptg_fwd	CTTTAATAAGGAGATATACCATGAAAGGACAAGAAACTCGTG	Gibson/NEB HiFi
Hptg_rev	TCTGTTCGACTTAAGCATTATCAGGAAACCAGCAGCTG	Gibson/NEB HiFi
gapa_fwd_pAYC_mcs2	TAATTAACCTAGGCTGCTG	Gibson/NEB HiFi
gapa_rev_pAYC_mcs2	ATGTATATCTCCTTCTTATACTTAAC	Gibson/NEB HiFi
gapa_fwd	TATAAGAAGGAGATATACATATGACTATCAAAGTAGGTATCAAC	Gibson/NEB HiFi
gapa_rev	GCAGCAGCCTAGGTTAATTATTATTTGGAGATGTGAGC	Gibson/NEB HiFi
pet28_tws_delc2_fwd	ctcgagcaccaccaccac	Gibson/NEB HiFi
pet28_tws_delc2rev	catatgtcctccggattggaag	Gibson/NEB HiFi
syNOSdelc2_178_1468_fwd	tccaatccggaggacatatgacctactcagaagccgtc	Gibson/NEB HiFi
syNOSdelc2_178_1468_fwd	tggtggtggtggtgctcgagctacaagttggctagccatttttc	Gibson/NEB HiFi
pet28_tws_delctt_fwd	tagctcgagcaccaccac	Gibson/NEB HiFi
pet28_tws_delctt_rev	catatgtcctccggattggaag	Gibson/NEB HiFi
syNOS_delctt1_1_1440_fwd	tccaatccggaggacatatgatgcttgtcaacgactctc	Gibson/NEB HiFi
syNOS_delctt1_1_1440_fwd	tggtggtggtgctcgagctagtagttgtctttctccacttg	Gibson/NEB HiFi
syNOS_K1412E_fwd	GCAAATTGCTgaaACAGAAGGAG	KLD
syNOS_K1412E_rev	ATAAATACCTCAAACACATTG	KLD
syNOS_T953A_fwd	GATCGGCAGCgcgGTCTATGAAC	KLD
syNOS_T953A_rev	CCTAGTACGGAATAGTTGAG	KLD
syNOS_K987A_fwd	CGACGAAATCgcgGGACAAGCCG	KLD
syNOS_K987A_rev	CCTTTATGTAGGGGAAC	KLD

Table S3. Primers used in the study with the cloning approach (left).

Domain	Couple	Potential (mV)	n	Calibrating dye (mV)
Globin	Fe^{3+}/Fe^{2+}	-250 ± 20	1	safranin T (-289, 12.5μM)
Fld	ox/hq	-173 ± 3	2	cresyl violet (-177.0, 60 μM)
FNR	ox/hq	-290 ± 13	2	safranin T (-289, 12.5 μM)

Table S4. Reduction potentials ($E^{0'}$) for $syNOS_{Glb}$, $syNOS_{Fld}$ and $syNOS_{FNR}$ vs. the Normal Hydrogen Electrode (NHE). For $syNOS_{Glb}$ the single electron reduction (n_e=1) from Fe^{3+} to Fe^{2+} was measured whereas for the flavin-containing domains a midpoint potential for the 2-electron reduction (n_e=2) from oxidized (ox) to hydroquinone (hq) was measured as no spectral signature for the semiquinone was apparent in the titrations. (n = 3 for all measurements)

Supplementary Figures

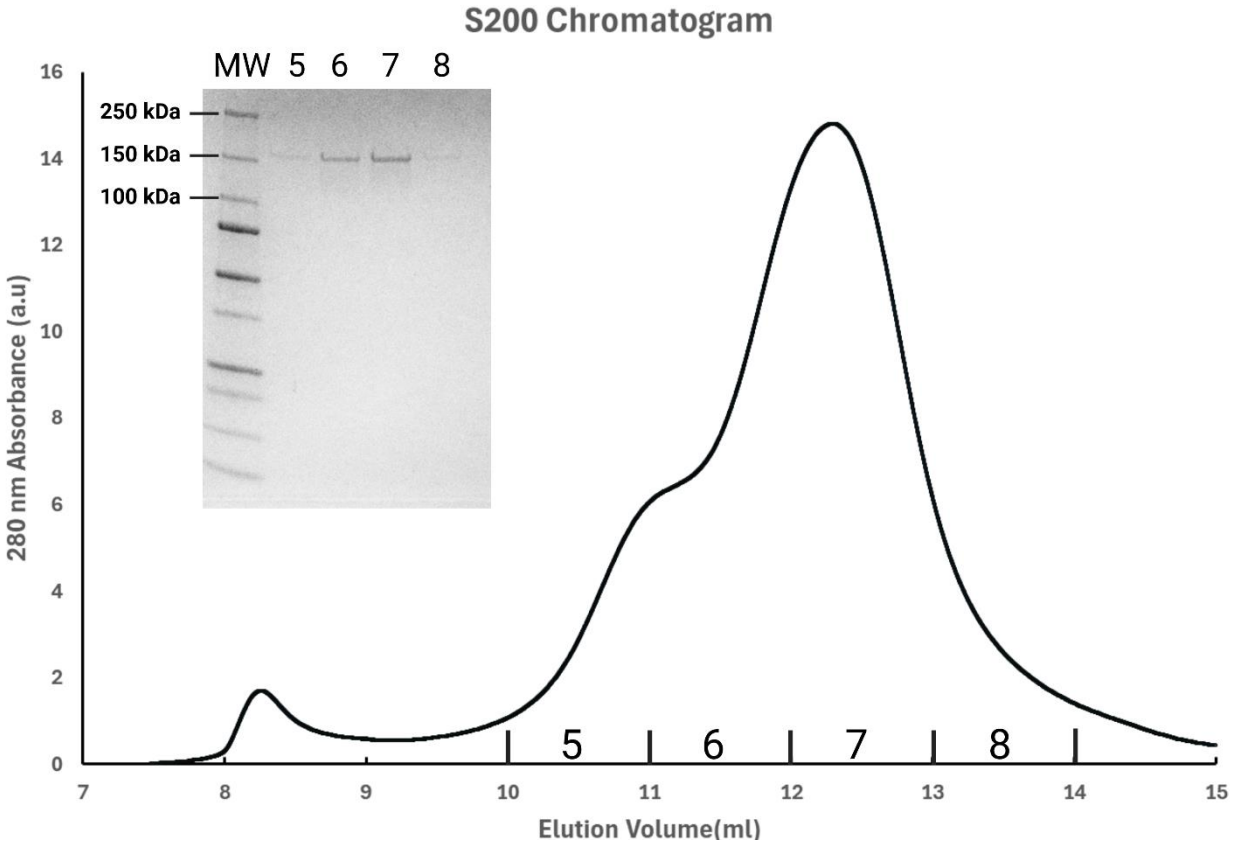

Figure S1. syNOS Purification. Representative chromatogram from a Superdex 200 increase 10/30 size exclusion chromatography column with an arrow denoting the syNOS dimer peak. The inset corresponds to a Coomassie blue stained 4-12% SDS-PAGE gel of fractions 5,6,7 and 8.

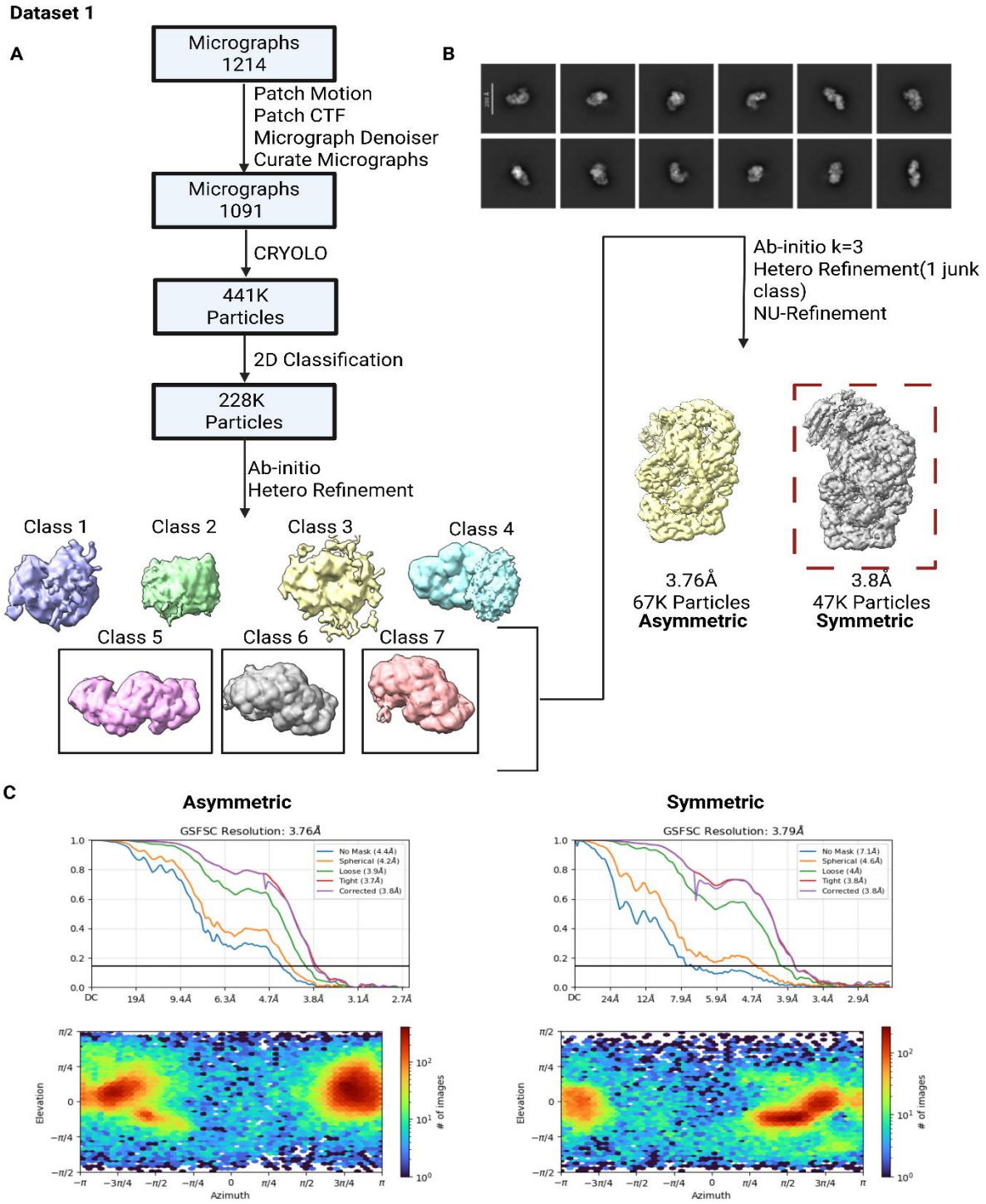

Figure S2. Dataset 1 processing scheme. (A) CryoEM processing workflow for dataset 1: syNOS ligand free. NOS-Sym class used for 3DVA and 3DFlex boxed (dashed-red). (B) Representative

954 2D Classes. CTF, contrast transfer function; NU, non-uniform refinement. (C) Overall Particle and

955 Gold-standard Fourier Shell Correlation (GSFSC) curves for NOS-Asym and NOS-Sym.

956

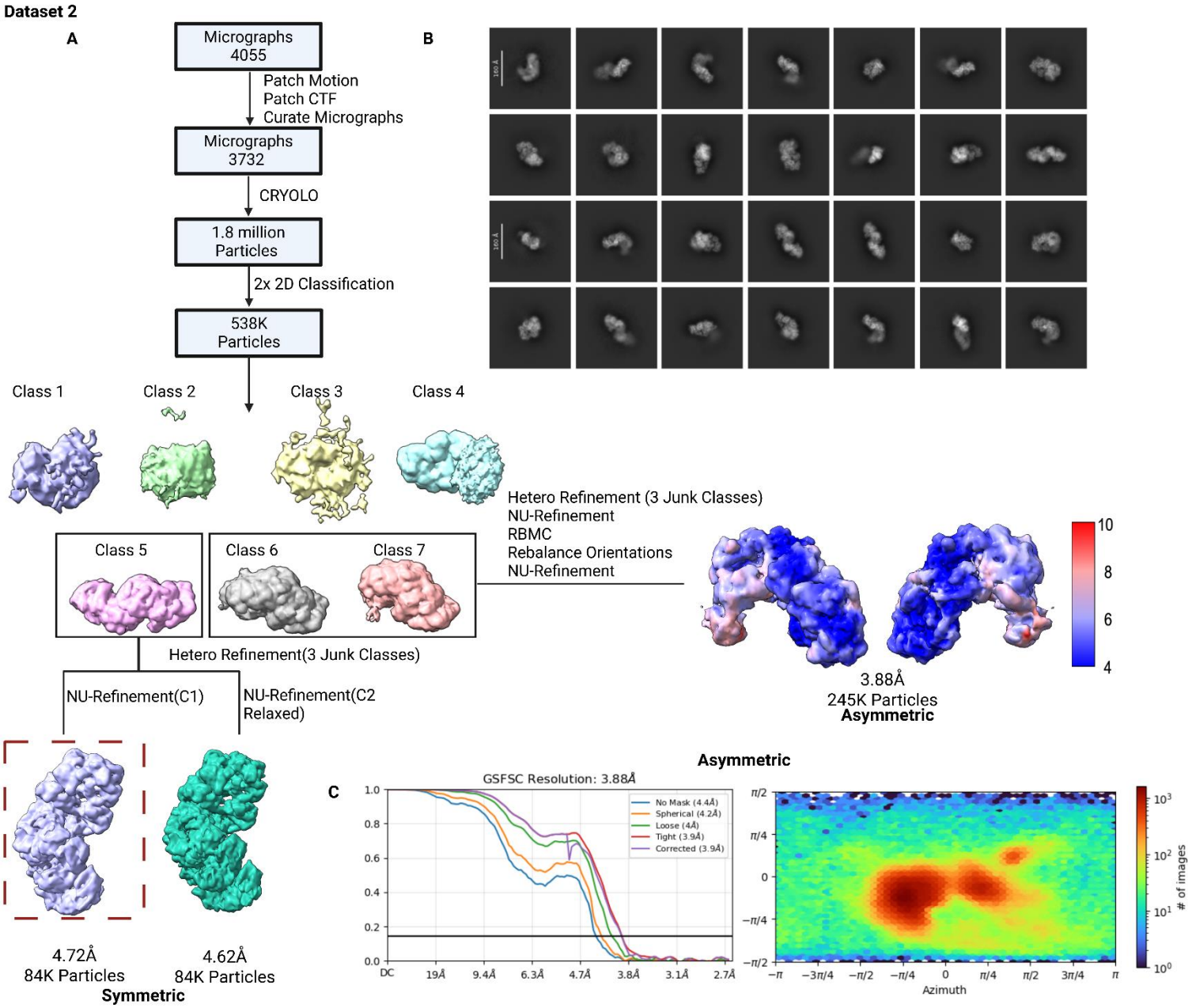

957

958 **Figure S3.** Dataset 2 processing scheme. (A) CryoEM processing workflow for dataset 2: syNOS
959 ligand free. NOS-Sym class used for 3DVA and 3DFlex boxed (dashed-red). (B) Representative 2D
960 Classes. (C) GSFSC curves and positional distribution of particles.

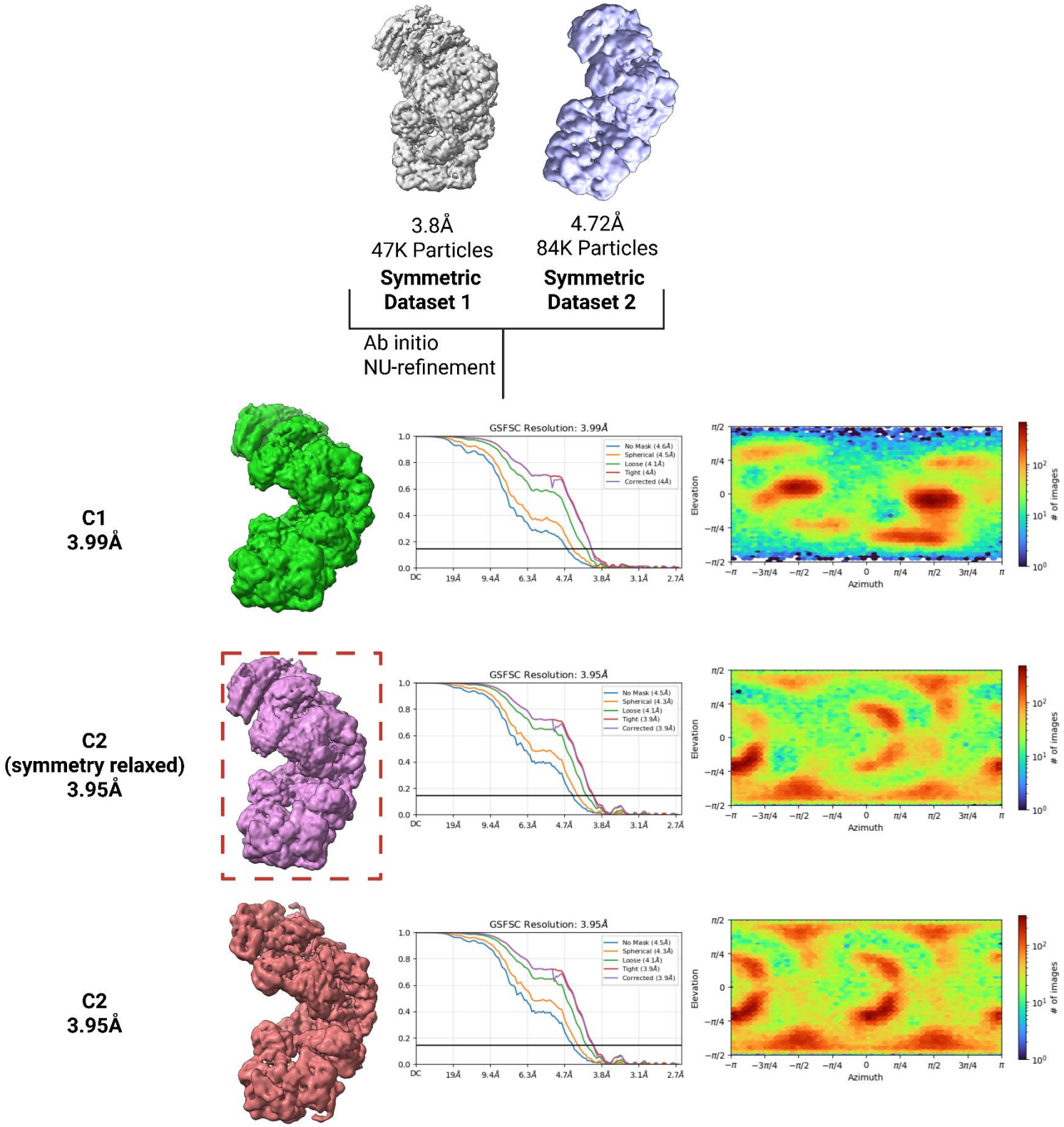

Figure S4. Merged data for NOS-Sym state, boxed class used for 3DVA and 3DFlex.

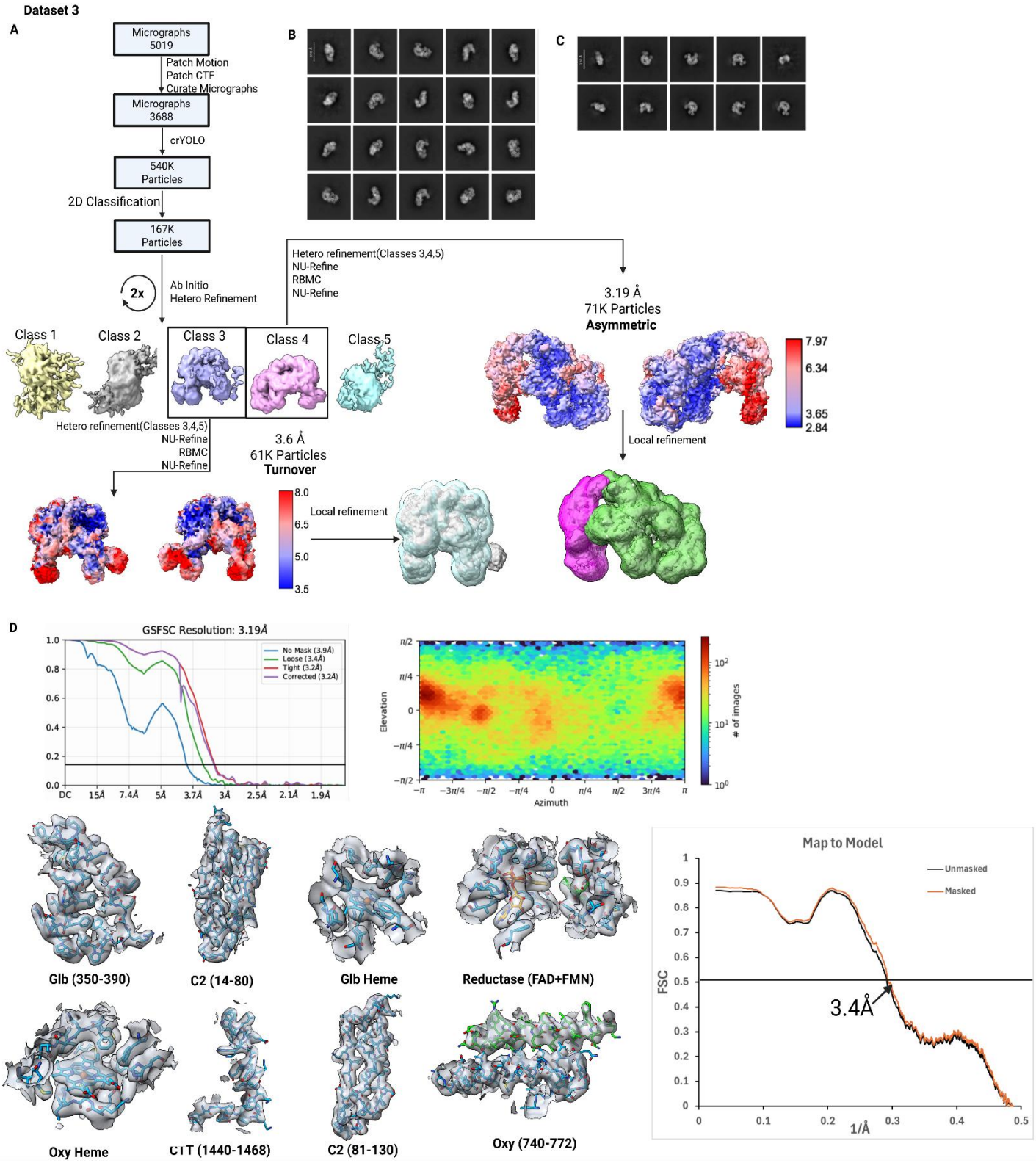

Figure S5. Dataset 3 processing scheme and validation. (A) CryoEM processing workflow for dataset 3: syNOS in the presence of Ca^{2+}/L-arginine (B) Representative 2D Classes for NOS-Asym

964 state (C) Representative 2D classes for NOS turnover state (NOS-TO_L) (D) Asymmetric states
965 GSFSC curves, orientation validation, model density fit and map to model Fourier Shell
966 Correlation (FSC).

967

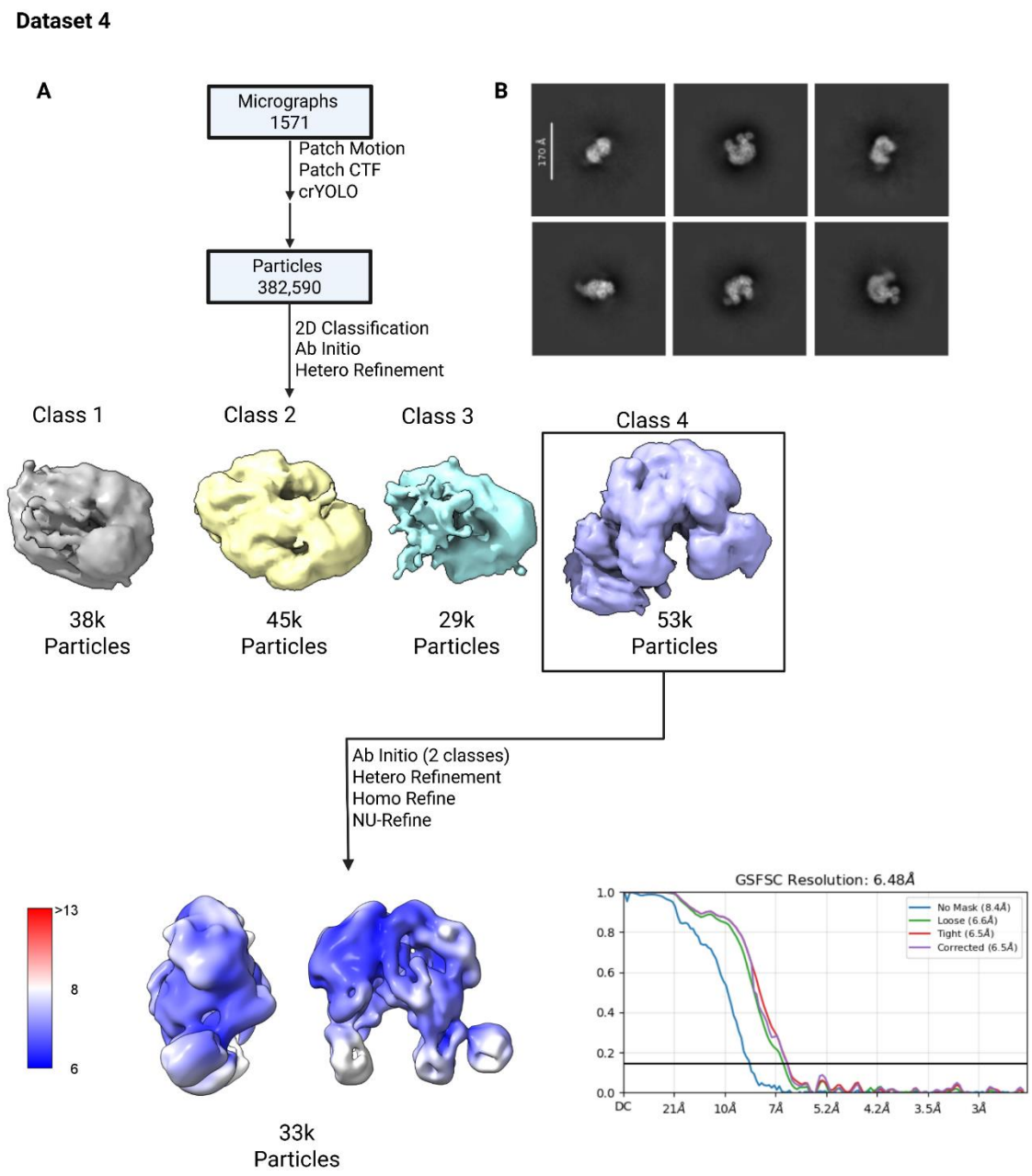

968

969 **Figure S6.** Dataset 4 processing scheme and validation. (A) CryoEM processing workflow for

970 dataset 4, syNOS with NADPH/Ca^{2+} including GSFSC curves. (B) Representative 2D classes for

971 NOS-TO_T.

Dataset 5

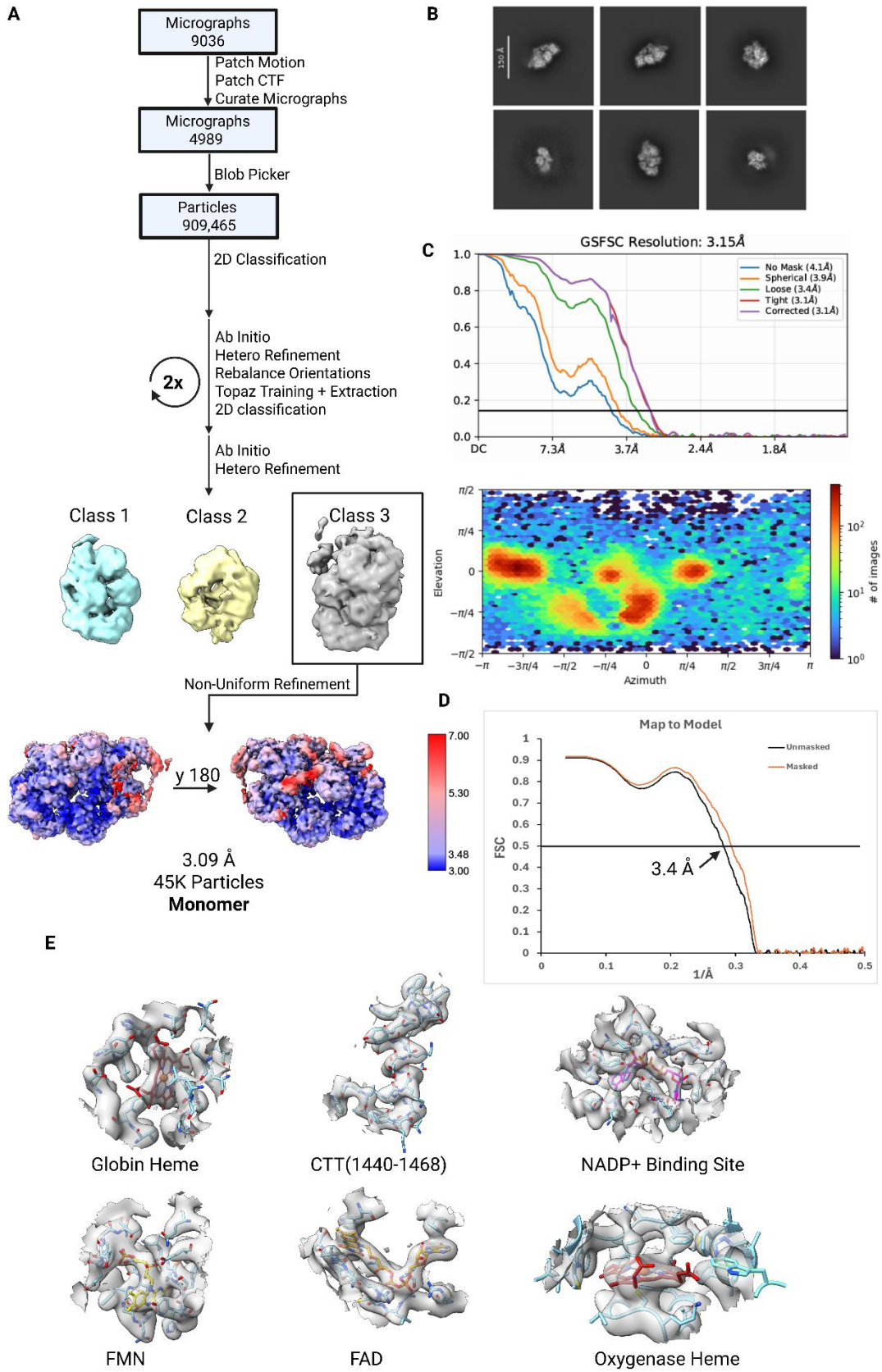
A
Micrographs 9036
Patch Motion
Patch CTF
Curate Micrographs
Micrographs 4989
Blob Picker
Particles 909,465
2D Classification
Ab Initio
Hetero Refinement
Rebalance Orientations
Topaz Training + Extraction
2D classification
2x
Ab Initio
Hetero Refinement
Class 1
Class 2
Class 3
Non-Uniform Refinement
y 180
3.09 Å
45K Particles
Monomer
B
150 Å
C
GSFSC Resolution: 3.15Å
No Mask (4.1Å)
Spherical (3.9Å)
Loose (3.4Å)
Tight (3.1Å)
Corrected (3.1Å)
DC
7.3Å
3.7Å
2.4Å
1.8Å
Elevation
Azimuth
# of images
D
Map to Model
Unmasked
Masked
FSC
3.4 Å
1/Å
E
Globin Heme
CTT(1440-1468)
NADP+ Binding Site
FMN
FAD
Oxygenase Heme

973 **Figure S7**. Dataset 5 processing scheme and validation. (A) CryoEM processing workflow for
974 dataset 5: syNOS with L-arginine, NADPH/Ca^{2+}/NADPH (B) Representative 2D classes for NOS-
975 Mon. (C) GSFSC curves, orientation validation and (D) Map to Model FSC. (E) Density fit of
976 model in map.

977

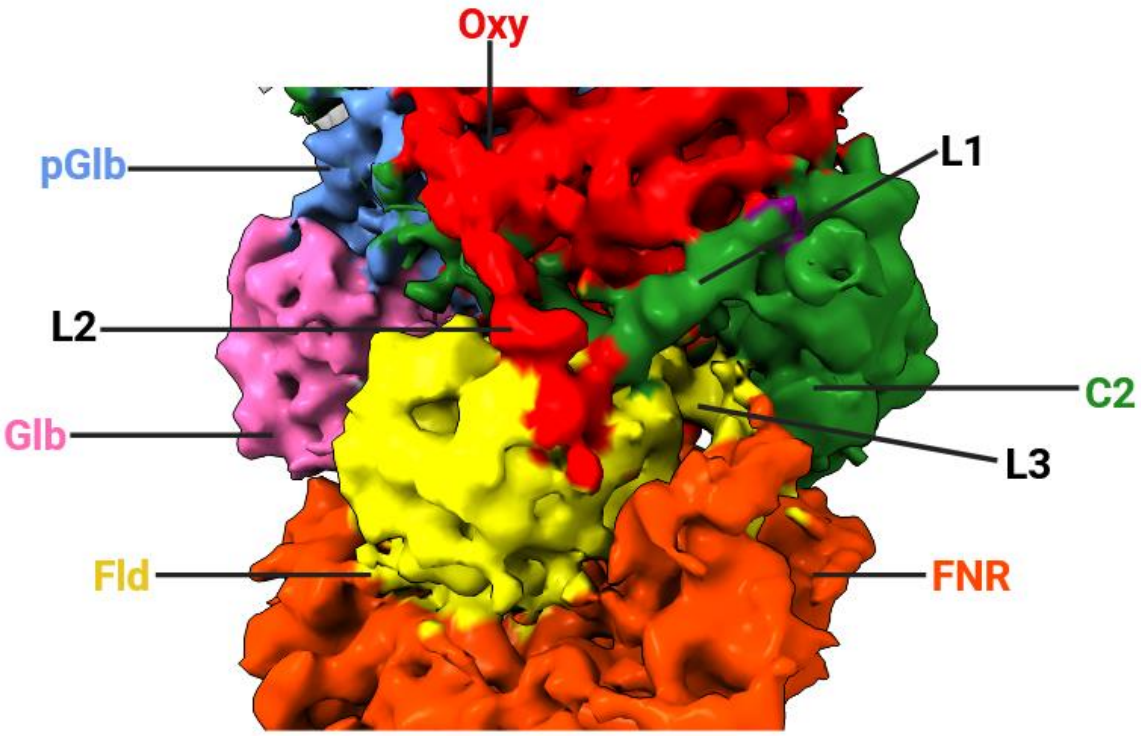

978

979 **Figure S8.** SyNOS linker intertwining. Intermediate resolution homodimer cryoEM density with
980 all three linkers colored the same as their preceding domains. Note how L1 threads beneath L2
981 and on top of L3. Movement of the C2 domain (green) will release the Fld module for NOS_{Oxy}
982 reduction.

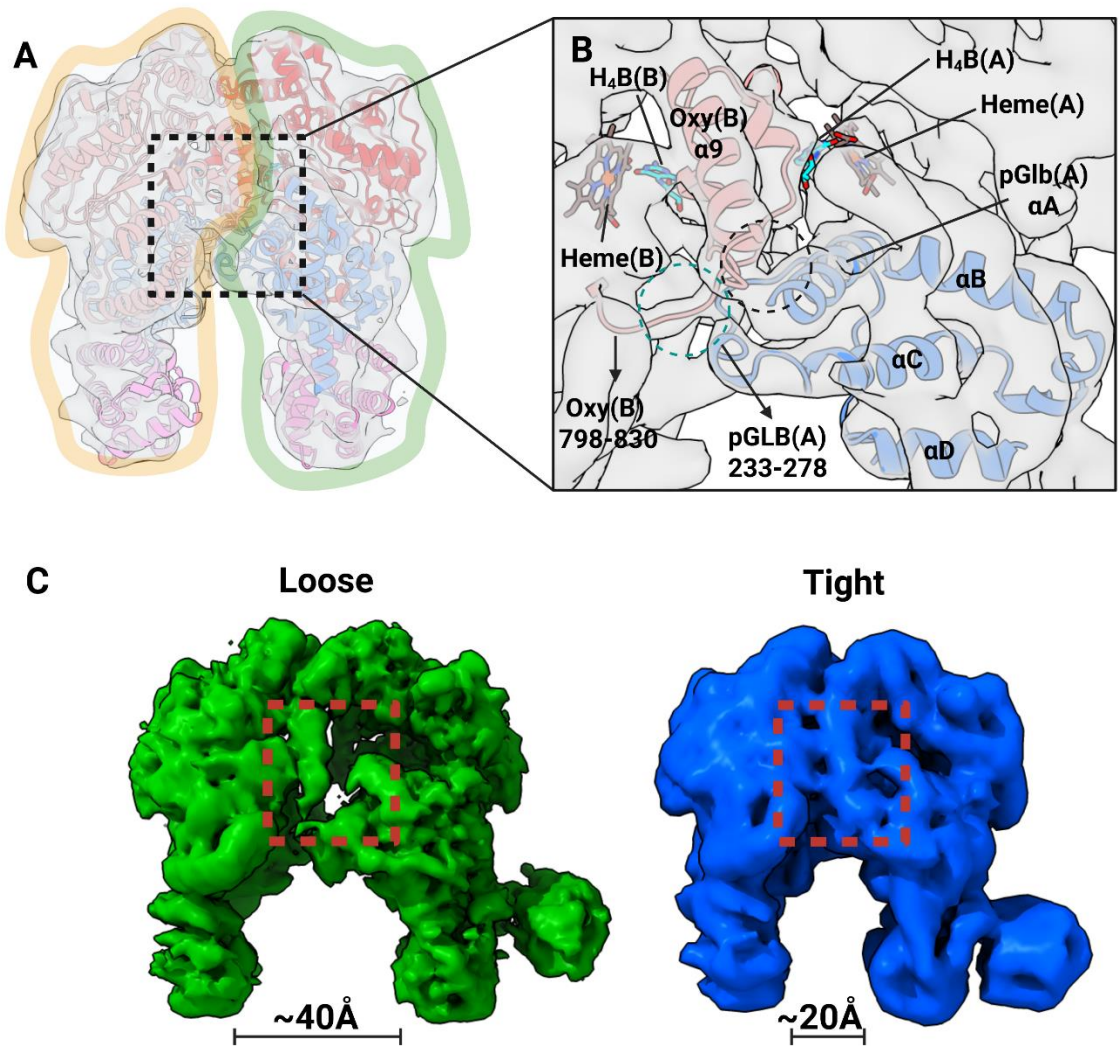

Figure S9. SyNOS tight and loose NOS_{Oxy} states. (A) syNOS cryoEM density (dataset 4) with the NOS_{Oxy} dimer interface outlined (orange and green) to show each subunit. (B) Close up of the dimeric interface showing the close association of NOS_{Oxy} α9 to an intersubunit pGlb C/D loop. Although at lower resolution, strong electron density for the core the NOS-TO_T interface includes the helical lariats and BH_4. (C) Loose (green) and tight (blue) NOS_{Oxy} dimers differ by a large 20 Å breathing motion normal to the dimer interface that also affects the positioning of the C2 domain (lower right peripheral electron density).

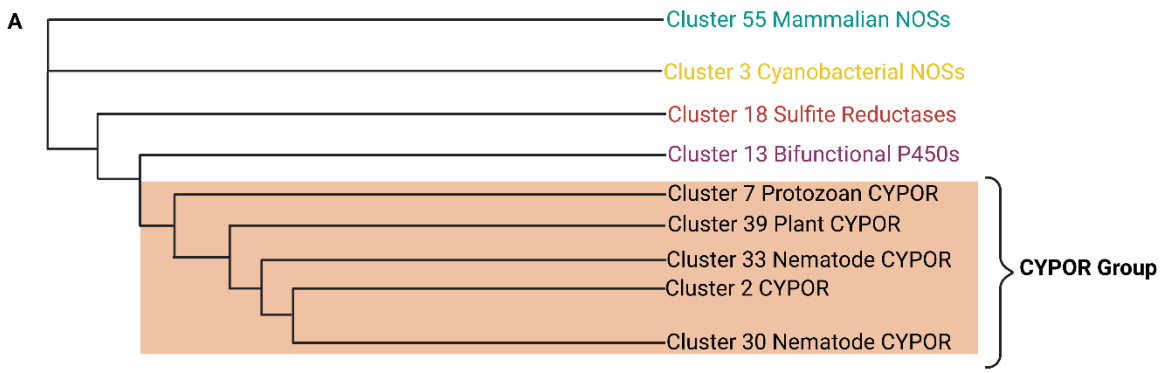

B

Cluster ID	Average Sequance Length	Standard Deviation of Sequence Length	Sequence Count
2	678	63	2521
39	702	49	1588
55	1117	103	278
3	1479	118	94
13	976	174	63
58	700	17	49
30	1126	283	47
7	638	35	45
18	601	74	44
33	652	36	44

Figure S10. Phylogenetic sequence clustering in the context of syNOS (residues 853-1468). Representative clusters were subjected to PhyML with clusters above 40 sequences represented in the tree. (B) Cluster composition by sequence length and count.

Figure S11. C-terminal tail (CTT) sequence alignment of syNOS, mNOSs and diatom NOS.

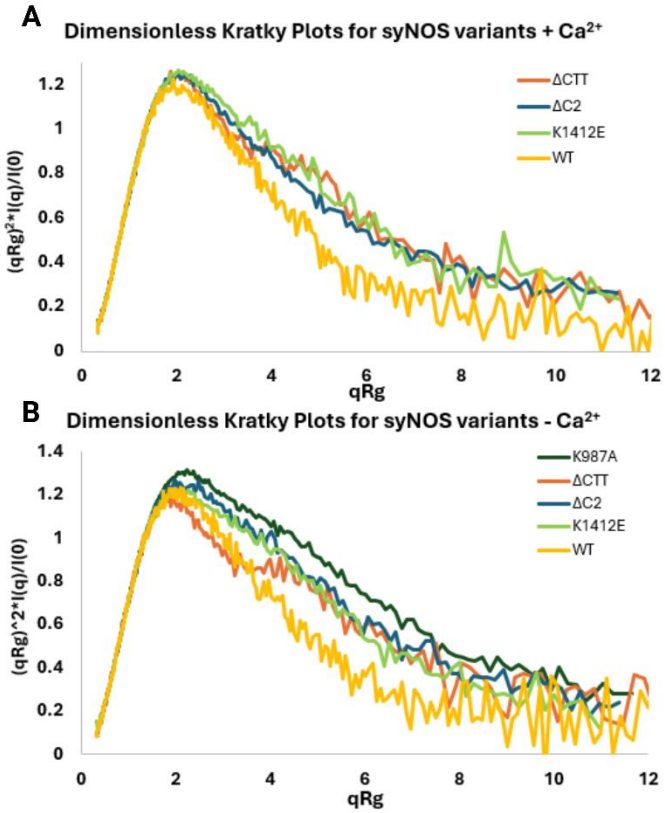

C

Sample	Rg [Guinier] (Å)	MW(Vc)	MW(Vp)
Predicted WT Dimer	55.59	-	-
Predicted WT Monomer	38.81	-	-
WT Ca^{2+}	52.83 ± 0.44	277.8	316.8
ΔC2 Ca^{2+}	56.89 ± 0.29	317.9	366.9
ΔCTT Ca^{2+}	62.71 ± 0.37	237.9	288.6
K1412E Ca^{2+}	57.16 ± 0.3	222	284
WT EGTA	52.83 ± 0.44	234.7	280.2
ΔC2 EGTA	57.34 ± 0.3	222.7	272.2
ΔCTT EGTA	61.18 ± 0.55	313.3	360
K1412E EGTA	55.28 ± 0.24	221.4	258.2
K987A EGTA	58.79 ± 0.37	213.6	266.7

Figure S12. SEC-SAXS of syNOS and variants. (A) Dimensionless Kratky plots, binned by 4 qRg values, for samples in the presence and absence of Ca^{2+}. (B) Table of predicted and experientially characterized radius of gyrations (Rgs) and molecular weights calculated either by volumes of correlation (V_C) or Porod volumes (V_P). (Samples were measured once)

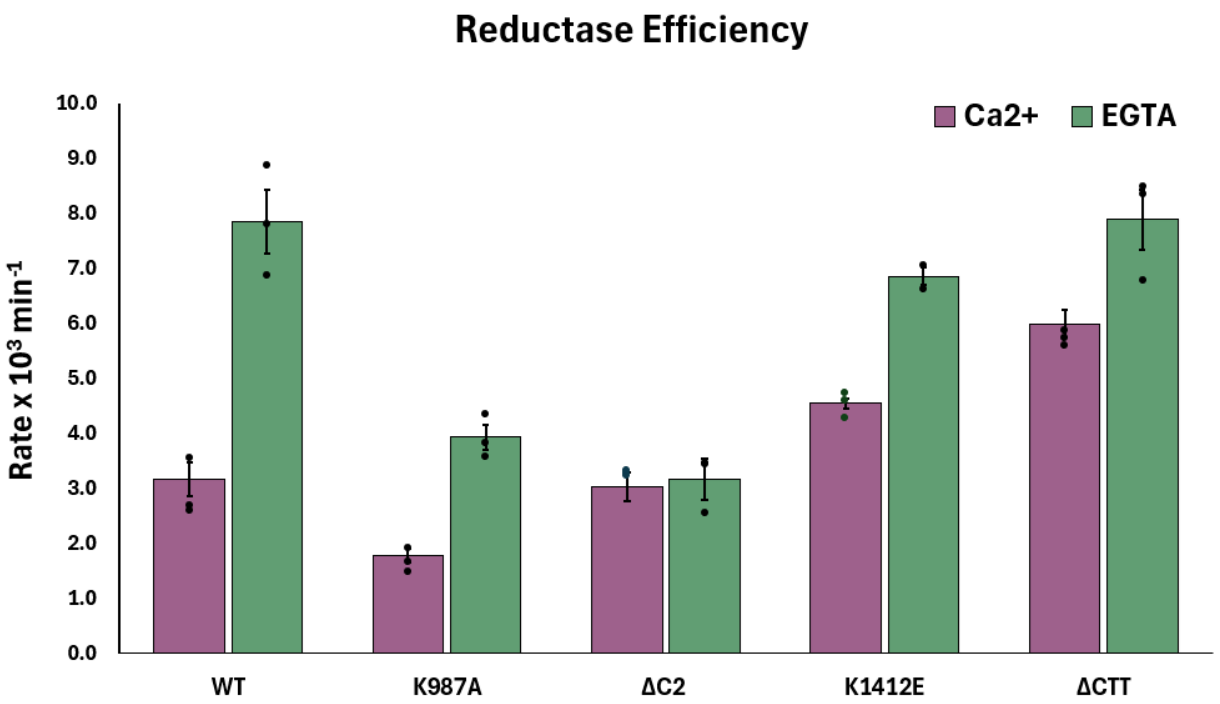

1008

1009 **Figure S13.** Steady state cytochrome c reductase activities of WT syNOS and variants expressed
1010 as turnover numbers (Cc reduced (NOS subunit)$^{-1}$ min^{-1}) with standard errors shown as error
1011 bars (see Methods). Statistical comparisons between groups were performed with a 2-way
1012 ANOVA with post hoc analysis using Tukey's multiple comparisons test. Significant differences
1013 are indicated as follows: ns (not significant), * ($p \leq 0.05$), ** ($p \leq 0.01$), *** ($p \leq 0.001$), **** ($p \leq$
1014 0.0001)..Ca:WT vs. Ca:K987A (ns); Ca:WT vs. Ca:ΔC2 (ns); Ca:WT vs. Ca:K1412E (ns); Ca:WT vs.
1015 Ca:ΔCTT (ns); Ca:WT vs. EGTA:WT (****) ; Ca:WT vs. EGTA:K987A (ns); Ca:WT vs. EGTA:ΔC2 (ns);
1016 Ca:WT vs. EGTA:K1412E (****); Ca:WT vs. EGTA:ΔCTT (****) ;Ca:K987A vs. Ca:ΔC2 (ns);
1017 Ca:K987A vs. Ca:K1412E (***); Ca:K987A vs. Ca:ΔCTT (****); Ca:K987A vs. EGTA:WT (**);
1018 Ca:K987A vs. EGTA:K987A (**); Ca:K987A vs. EGTA:ΔC2 (ns); Ca:K987A vs. EGTA:K1412E (****);
1019 Ca:K987A vs. EGTA:ΔCTT (****); Ca:ΔC2 vs. Ca:K1412E (ns); Ca:ΔC2 vs. Ca:ΔCTT (**); Ca:ΔC2 vs.
1020 EGTA:WT (****); Ca:ΔC2 vs. EGTA:K987A (ns); Ca:ΔC2 vs. EGTA:ΔC2 (ns); Ca:ΔC2 vs.
1021 EGTA:K1412E (****); Ca:ΔC2 vs. EGTA:ΔCTT (****);Ca:K1412E vs. Ca:ΔCTT (ns); Ca:K1412E vs.
1022 EGTA:WT (****); Ca:K1412E vs. EGTA:K987A (ns); Ca:K1412E vs. EGTA:ΔC2 (ns); Ca:K1412E vs.
1023 EGTA:K1412E (**); Ca:K1412E vs. EGTA:ΔCTT (****); Ca:ΔCTT vs. EGTA:WT (**); Ca:ΔCTT vs.
1024 EGTA:K987A (*); Ca:ΔCTT vs. EGTA:ΔC2 (***); Ca:ΔCTT vs. EGTA:K1412E (ns); Ca:ΔCTT vs.

1025 EGTA:ΔCTT (**); EGTA:WT vs. EGTA:K987A (****); EGTA:WT vs. EGTA:ΔC2 (****); EGTA:WT vs.
1026 EGTA:K1412E (ns); EGTA:WT vs. EGTA:ΔCTT (ns); EGTA:K987A vs. EGTA:ΔC2 (ns); EGTA:K987A vs.
1027 EGTA:K1412E (***); EGTA:K987A vs. EGTA:ΔCTT (***); EGTA:ΔC2 vs. EGTA:K1412E (****);
1028 EGTA:ΔC2 vs. EGTA:ΔCTT (****); EGTA:K1412E vs. EGTA:ΔCTT (ns). (n=3, except for K1412E
1029 +EGTA; n = 2).

1030

A

Reductase	λ_{obs}	A_1 (%)	k_{obs1} (s^{-1})	A_2 (%)	k_{obs2} (s^{-1})	A_3 (%)	K_{obs3} (s^{-1})	
$syNOS_{Red}$(-Ca^{2+})	450	89	178 (± 0.78)	11	4.12 (± 0.03)	-	-	This study
$syNOS_{FL}$(-Ca^{2+})	450	63	2.38 (± 0.03)	37	0.004 (± 0.001)	-	-	This study
$nNOS_{Red}$(-CAM)	458	28	57 (± 1)	52	5.2 (± 0.1)	20	570 (± 41)	Craig et al.[17]
$nNOS_{Red}$(+CAM)	458	44	608 (± 66)	56	86 (± 2)	-	-	Craig et al.[17]
CYPOR	450	90	42 (± 4)	10	3.8 (± 0.5)	-	-	Hamdane et al.[68]

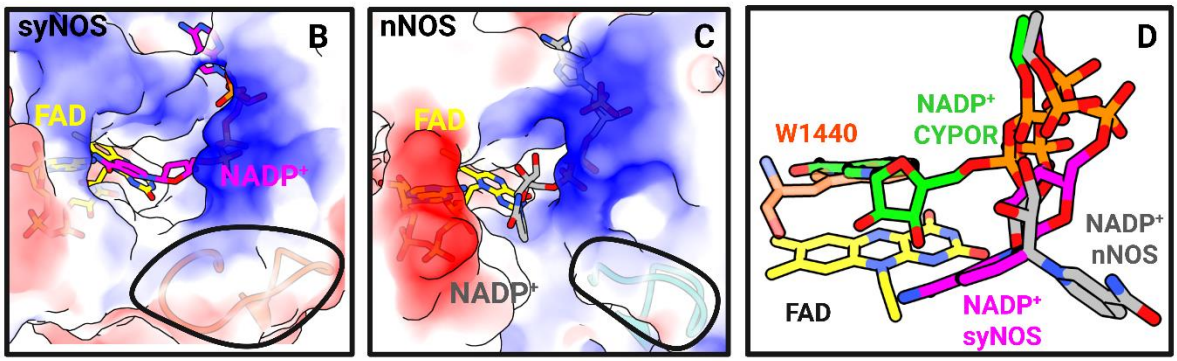

1031

1032 **Figure S14.** Flavin reduction by NADPH. (A) Table of flavin reduction rate constants for syNOS,
1033 nNOS and CYPOR(n = 4). (B) Surface representation and model of $NADP^+$ (magenta) bound in
1034 the pocket of syNOS-Mon with loop 1050-1062 (orange-red and circled in black) in comparison
1035 to (C) nNOS bound to $NADP^+$ (grey) with corresponding loop 1002-1012 (aqua) circled Iin black.
1036 (D) Overlay of $NADP^+$ bound conformations of syNOS, nNOS and CYPOR W677X (1-676) (PDB:
1037 1JA0) (green) over a consensus position of FNR-bound FAD (yellow). syNOS CTT residue 1440
1038 blocks access of the nicotinamide ring to the isoalloxazine ring.

1039

1040

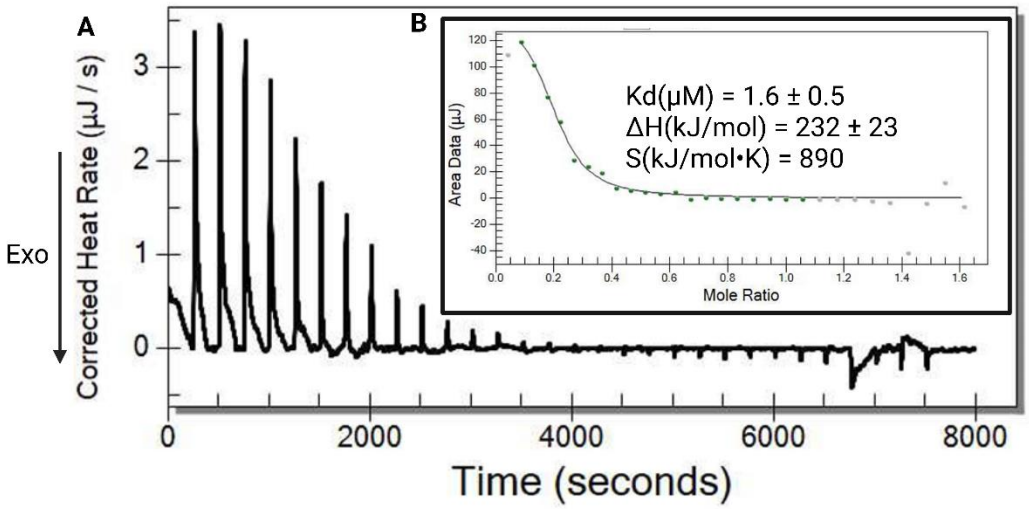

Figure S15. Isothermal calorimetric titration of Ca^{2+} with $syNOS_{C2}$ (residues 1-138). (A) Endothermic, baseline corrected isotherm of Ca^{2+} titrated into $syNOS_{C2}$. (B) Binding model fit with the accompanying thermodynamic parameters. (Samples were measured once)

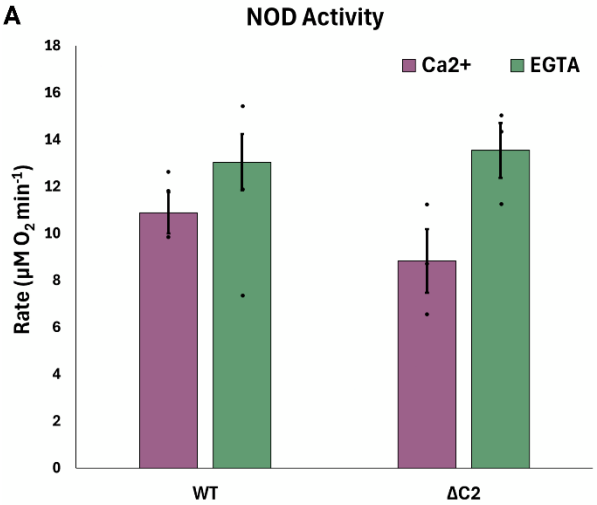

B

Variant	Condition	Rate Constant (s^{-1})
WT	Ca	0.33 (± 0.02)
ΔC2		0.54 (± 0.05)
WT	EGTA	0.22 (± 0.02)
ΔC2		0.35 (± 0.03)

Figure S16. SyNOS globin-based NOD activity and heme reduction rates. (A) NOD activity was measured by O2 consumption in the presence of the NO-donor NOC-7 and NADPH for WT and $syNOS_{\Delta C2}$ (n=3, except for $syNOS_{\Delta C2}$ + Ca^{2+} ; n = 2). (B) Heme reduction rate constants of $syNOS_{Glb}$ in the presence or absence of Ca^{2+} for WT or $syNOS_{\Delta C2}$, with standard error

represented. Statistical comparisons between groups were performed with a 2-way ANOVA with post hoc analysis using Tukey's multiple comparisons test, all comparisons were non-significant.

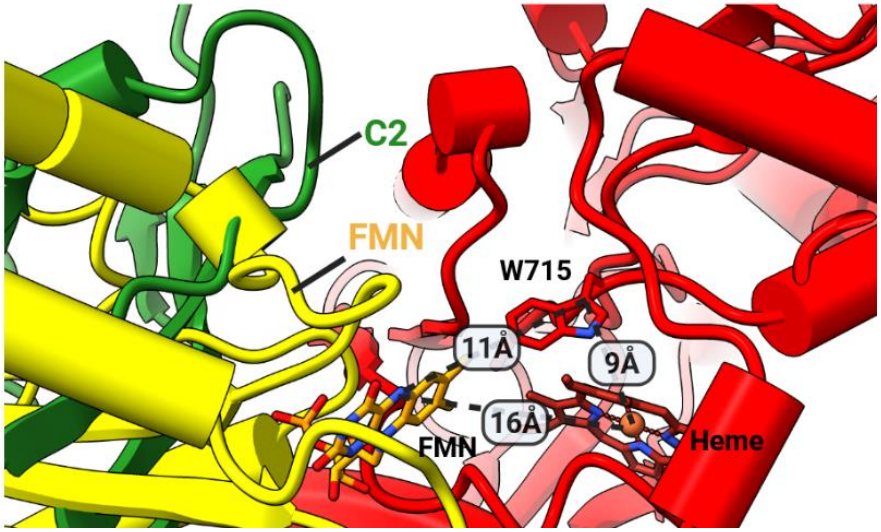

Figure S17. Output state predicted by AlphaFold3 with FMN-to-Trp715-to-Heme distances shown. Overlay of the C2 in the locked state (green) with the output Fld conformation (yellow) illustrates that the Fld is sterically blocked by the C2 domain in the NOS-Asym state.

1065

1066

1067

1068